Research paper

Ionic displacement of Ca^{2+} by Pb^{2+} in calmodulin is affected by arrhythmia-associated mutations

Valerio Marino [1], Giuditta Dal Cortivo [1], Daniele Dell'Orco [*]

Department of Neurosciences, Biomedicine and Movement Sciences, Section of Biological Chemistry, University of Verona, I-37134 Verona, Italy

ARTICLE INFO

ABSTRACT

Lead is a highly toxic metal that severely perturbs physiological processes even at sub-micromolar levels, often by disrupting the Ca^{2+} signaling pathways. Recently, Pb^{2+}-associated cardiac toxicity has emerged, with potential involvement of both the ubiquitous Ca^{2+} sensor protein calmodulin (CaM) and ryanodine receptors. In this work, we explored the hypothesis that Pb^{2+} contributes to the pathological phenotype of CaM variants associated with congenital arrhythmias. We performed a thorough spectroscopic and computational characterization of CaM conformational switches in the co-presence of Pb^{2+} and four missense mutations associated with congenital arrhythmias, namely N53I, N97S, E104A and F141L, and analyzed their effects on the recognition of a target peptide of RyR2. When bound to any of the CaM variants, Pb^{2+} is difficult to displace even under equimolar Ca^{2+} concentrations, thus locking all CaM variants in a specific conformation, which exhibits characteristics of coiled-coil assemblies. All arrhythmia-associated variants appear to be more susceptible to Pb^{2+} than wild type (WT) CaM, as the conformational transition towards the coiled-coil conformation occurs at lower Pb^{2+}, regardless of the presence of Ca^{2+}, with altered cooperativity. The presence of arrhythmia-associated mutations specifically alters the cation coordination of CaM variants, in some cases involving allosteric communication between the EF-hands in the two domains. Finally, while WT CaM increases the affinity for the RyR2 target in the presence of Pb^{2+}, no specific pattern could be detected for all other variants, ruling out a synergistic effect of Pb^{2+} and mutations in the recognition process.

1. Introduction

Lead toxicity is a serious global health problem as lead, like other heavy metals, slowly accumulates in the air, water, and soil [1], due to its massive employment in agriculture and industry [2]. Upon accumulating in the environment, where it can persist for centuries, lead enters in the food chain through terrestrial and marine fauna and flora [3], ultimately reaching humans mainly through inhalation and ingestion. Occupational workers, children and pregnant women are the most susceptible categories to lead poisoning [4], together with people affected by Ca^{2+}-deficiency and with a low dietary Ca^{2+}-intake, such as refugees, elderly and children. Once introduced to the human body

through the diet, lead can be excreted, although the largest part of it accumulates in the bones, displacing Ca^{2+} in osteocalcin [5].

The most common cationic dissociated form of lead (Pb^{2+}) is transported in the blood stream throughout the human body, thus its concentration (Blood Lead Level, BLL) can be used as a prognostic index for lead poisoning, which is defined at a BLL of 25 µg/dl and 5 µg/dl, for adults and children, respectively (Center for Disease Control and Prevention, CDCP, 2014), while the current exposure threshold recommended by the CDCP is <5 µg/dl, which corresponds to 185 nM. Relatively low amounts of Pb^{2+} can therefore trigger severe toxic effects.

As in the case of other heavy metals, lead toxicity is normally manifested through the perturbation of a variety of biochemical and

physiological mechanisms, thus causing a multiplicity of symptoms among which: i) neurological disorders related to the central and peripheral nervous systems [6,7]; ii) developmental defects [8,9]; iii) anemia [10]; iv) hypertension [11]; v) nephrotoxicity [12]; vi) bone loss [4], and vii) carcinogenicity [13]. A strict interconnection between Ca^{2+}-signaling and Pb^{2+} (neuro) toxicity has been recently postulated [14], and the most accredited hypothesis on the pathogenic mechanism underpinning lead poisoning is ion mimicry. Pb^{2+} and Ca^{2+} have in fact the same charge and similar ionic radii (0.99 Å for Ca^{2+} and 1.20 Å for Pb^{2+}), which would allow ion binding with the same requirements in terms of coordination number [15] and geometry [16]. Moreover, the similarity with Ca^{2+}-ions would permit Pb^{2+} to enter the cells through Ca^{2+}-dedicated channels [17,18], where several lines of evidence demonstrated that it could substitute for Ca^{2+} in several proteins [19–23], thus acting as a potential alternative second messenger [24].

Ca^{2+}-binding proteins bind Pb^{2+} with high affinity predominantly via the canonical EF-hand Ca^{2+}-binding motifs [25]. The prototypical Ca^{2+}-sensor Calmodulin (CaM), as well as troponin C, and oncomodulin [19] have been shown to bind Pb^{2+} in a preferential manner with respect to Ca^{2+}.

CaM is a ~17 kDa ubiquitously expressed Ca^{2+}-sensor which, upon binding Ca^{2+} ions in each of the four functional EF-hands, undergoes a major structural rearrangement from a closed to an open conformation [26–29] (see Fig. 1), which is then able to bind and regulate over 300 molecular targets [30].

The role of CaM in lead toxicity has been under investigation for over 40 years [22,31], and it likely occurs via the Pb^{2+}-mediated dysregulation of its numerous effectors. Indeed, it has been proven that in resting cells where Ca^{2+}-concentration is particularly low (10^{-7} M), Ca^{2+}-sensor proteins can bind other divalent cations including Pb^{2+}, which can bind to all four EF-hand binding sites [26], thus leading to improperly activated CaM.

Beside Ca^{2+}-displacement by Pb^{2+}, opportunistic binding has been recently proposed as an alternative pathogenic mechanism by Kirberger et al. in their study on the structural analogies between Ca^{2+} and Pb^{2+} binding sites [32], which led to the conclusion that any protein site
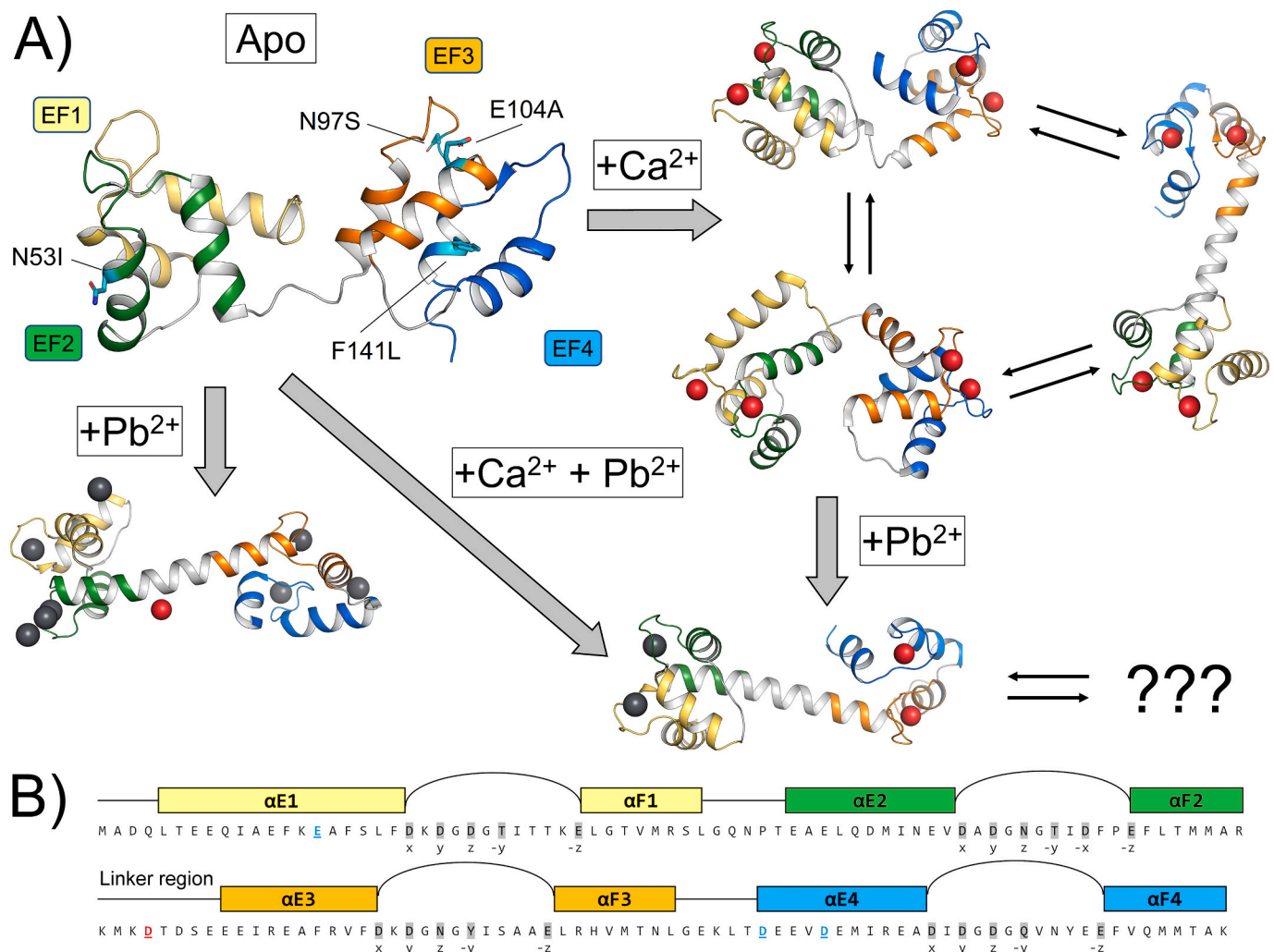
Fig. 1. Schematic representation of CaM conformational plasticity and ion coordination. A) The three-dimensional structure of CaM in its apo, "closed" conformation (PDB entry 1DMO [27]), Ca^{2+}-bound open conformation (PDB entries 1CLL [28]), Ca^{2+}-bound closed conformation (PDB entry 2K0E [29], 2 conformers from the NMR ensemble), Pb^{2+}-bound (PDB entry 2V01 [49]), and Pb^{2+}/Ca^{2+}-bound intermediate form. In all states, CaM is represented as cartoons with EF1 motif colored in yellow, EF2 in green, EF3 in orange and EF4 in blue. Ca^{2+} and Pb^{2+} ions are shown as red and grey spheres, respectively, residues mutated in arrhythmia-associated variants are represented as cyan sticks with N atoms in blue and O atoms in red. B) CaM sequence is shown together with the organization in structural motifs, αE*n* and αF*n* indicate the entering and exiting helix of EF-hand motif *n*, each EF-hand is colored according to panel A, the linker region is labelled. Residues involved in both Ca^{2+} and Pb^{2+} binding are shaded in grey and labelled with the respective position according to the canonical Ca^{2+}/Pb^{2+} coordination. Residue D78, involved in opportunistic Ca^{2+} binding, is shown in bold, underlined, and colored in red. Residues involved in opportunistic Pb^{2+} binding are shown in bold, underlined, and colored in blue.

containing negatively charged residues might coordinate Pb^{2+}-ions, such as in the case of the DTDSEEE stretch in the linker region of CaM (Fig. 1). These results suggest that Pb^{2+} can adapt to structurally heterogeneous binding geometries, thus implying that opportunistic binding may indeed play an active role in metal toxicity [32]. Even though opportunistic binding of Pb^{2+} has been demonstrated for CaM by NMR experiments [33], ionic displacement is the most probable mechanism explaining the toxic effects of heavy metals on other Ca^{2+}-sensor proteins, such as Neuronal Calcium Sensor 1 (NCS1) [34] and Downstream Regulatory Element Antagonist Modulator (DREAM) [35], and on the modulation of the interaction with their targets.

Recently, Pb^{2+} was also found to alter the functionality of Ryanodine Receptors (RyR), a class of CaM-regulated intracellular Ca^{2+} channels capable of binding Ca^{2+}, and responsible for preserving Ca^{2+}-homeostasis [36]. RyRs can be classified in 3 subgroups with specific localization, RyR1 is mainly expressed in skeletal muscle and cerebellar Purkinje neurons [37], RyR2 is mostly present in cardiomyocytes and in the brain [38], while RyR3 is brain specific [39]. Pb^{2+} was shown to modulate the binding of ryanodine to RyR2 and RyR3, resulting in a significant depression of Ca^{2+}-oscillations [40] and causing an increase of intracellular $[Ca^{2+}]$ in rats by inducing the overexpression of RyR2 and RyR3 [41]. Overall, these recent findings suggest that RyRs may be the target of Pb^{2+}-induced neurotoxicity through impaired Ca^{2+}-signaling.

Besides the established neurotoxic effect, Pb^{2+} is known to perturb cardiac functionality affecting heart rate, contraction, excitability, and rhythm, through still partially undisclosed mechanisms [42], therefore suggesting Pb^{2+} exposure as a relevant risk factor for cardiac diseases. The dysregulation of RyRs-mediated Ca^{2+}-release has been associated over the last 10 years with potentially lethal diseases affecting both cardiac and skeletal muscle [43]. In this regard, it is relevant that 17 missense variants of CaM have been associated with heart failure and sudden cardiac death [44] due to long QT syndrome (LQTS) and Catecholaminergic Polymorphic Ventricular Tachycardia (CPVT) [45].

The potential involvement of both CaM and RyR2 in Pb^{2+}-associated cardiac toxicity raised the question of whether CaM could be at least partially responsible for the pathological phenotype, due to alterations in its conformational switch or in the recognition of the target. In this work, we questioned if arrhythmia-associated variants of CaM could be differently susceptible to Pb^{2+}, thus suggesting a further potential risk factor for lead poisoning. To this end, we performed a thorough biophysical and biochemical study on the structural properties of five CaM variants with distinct structural location and role, namely: i) (WT; ii) N53I, located in the entering helix of EF2 (αE2, Fig. 1) and associated with CPVT; iii) N97S, belonging to the ion-binding loop of EF3, involved in ion coordination via the backbone carbonyl group (Fig. 1) and associated with CPVT and LQTS [45]; iv) E104A, located in the ion-binding loop of EF3 [46], responsible for ion coordination through the sidechain carboxyl group and found in LQTS patients; v) F141L, also found in LQTS patients [47], located in αF4 and responsible for the hydrophobic packing of helices αE4 and αF4. Finally, we investigated the effects of Pb^{2+} on the interaction between CaM variants and RyR2, focusing on a 31-residue peptide encompassing the R3581-L3611 region of RyR2 [48] known as CaM binding domain 2 (CaMBD2).

2. Materials and methods

2.1. Materials

Ethylenediaminetetraacetic acid (EDTA), Tris(hydroxymethyl)aminomethane (TRIS), KCl, $CaCl_2$, $Pb(NO_3)_2$, and 8-Anilinonaphthalene-1-sulfonic acid (ANS) were purchased from Merck and were of the highest purity grade available.

2.2. Protein purification

CaM variants N53I, N97S, E104A, and F141L (residue numbering refers to the mature proteins that lack the Met in position 1) were heterologously expressed in *E. coli* and purified by reverse immobilized metal affinity chromatography as previously described [50,51]. Briefly, the cDNA of human WT CaM (Uniprot entry: P0DP23) was cloned into a pET24a (+) vector containing a 6 x His-tag and the Tobacco Etch Virus protease recognition site at the N-terminus. Cloning, codon optimization, site-directed mutagenesis and sequence check were performed by Genscript. All CaM variants were extracted by the soluble fraction using a His-trap FF Crude column (GE) and, after His-tag removal, proteins were flash-frozen in working buffer (20 mM TRIS pH 7.5, 150 mM KCl) and stored at −80 °C until use.

The portion of human Ryanodine Receptor 2 (RyR2) used in the present study, representing the CaMBD2 region, encompasses the R3581-L3611 amino acid stretch (RSKKAVWHKLLSKQRKRAVVACFR-MAPLYNL) and was purchased from Genscript as lyophilized powder (purity >95 %, assessed via mass spectrometry and HPLC).

2.3. Limited proteolysis

Limited proteolysis was performed incubating 26.6 μM CaM variants in the presence of 0.4 μM trypsin (ratio 1:66) in four different conditions: apo (200 μM EDTA), Pb^{2+}-bound (100 μM EDTA + 200 μM Pb^{2+}, free Pb^{2+} ~100 μM), Ca^{2+}-bound (500 μM Ca^{2+}) and in co-presence of Ca^{2+} and Pb^{2+} (500 μM Ca^{2+} + 100 μM Pb^{2+}). A time scan was performed first for WT CaM, setting the temperature at 25 °C and collecting sample at different times from 0 to 90 min, leading to the selection of 10 min as the optimal incubation time for the resolution of the proteolytic fragments. Limited proteolysis for each CaM variant was performed at both 25 °C and 37 °C, reactions were blocked by adding sample buffer 4× and by incubating the samples at 95 °C for 10 min, finally samples were loaded on 15 % SDS-PAGE and Coomassie Blue-stained.

2.4. Circular dichroism spectroscopy

Variations in the secondary structure of CaM variants were assessed by circular dichroism (CD) in the far-UV, as previously described [50,51]. Spectra were collected on a Jasco J-710 provided with a Peltier-type thermostated cell holder, after setting temperature at 37 °C, response time at 4 s, bandwidth at 5 nm, and data pitch at 1 nm. For each variant/ion combination, 4 accumulations of the spectra were recorded, the spectrum of the buffer (20 mM TRIS pH 7.5, 150 mM KCl) was considered as blank and subtracted. Protein concentration was quantified before each measurement by Bradford assay [52]. Far-UV CD spectra (200–250 nm) were recorded using a 1-mm pathlength quartz cuvette containing 10 μM CaM variants in decalcified buffer and in the presence of 200 μM Ca^{2+}, 200 μM Pb^{2+}, or 200 μM Pb^{2+} and 200 μM Ca^{2+}. The effects of Ca^{2+} on the conformational transitions affecting the secondary structure of CaM variants upon Pb^{2+}-titration were evaluated by monitoring the ratio between the ellipticity at 222 and 208 nm (θ_{222} / θ_{208}), the typical minima exhibited by all α-helix proteins. Briefly, 10 μM CaM variants were titrated with increasing concentration of Pb^{2+} (0–320 μM) in the absence and in the presence of 200 μM Ca^{2+} for a total of three technical replicates for each variant. Each titration was fitted to a 4-parameter Hill sigmoid ($\frac{\theta_{222}}{\theta_{208}} = b + \frac{\Delta r * x^h}{EC_{50}{}^h + x^h}$), where b is the starting baseline of the titration in terms of θ_{222} / θ_{208}, Δr is the variation of the ratio at 0 and 320 μM $[Pb^{2+}]$, corresponding to the starting and the end point of the titration, respectively, h is the Hill coefficient, and EC_{50} is the effective Pb^{2+}-concentration at which the conformational transition is half-maximal. Values reported in Table 1 refer to the average ± standard deviation of the values obtained from each titration shown in Fig. 4. The statistical significance of the differences between EC_{50} values for each variant/state combination was assessed by two-tailed *t*-tests.

Table 1
Results from CD spectroscopy.

Variant	State	$\theta_{222}/\theta_{208}$ [a]	$\Delta\theta_{222}/\theta_{222}$ [b]	EC_{50} (μM) [c]	Hill coefficient
WT	Apo	0.90	–	69.8 ± 21.0	1.3 ± 0.3
	Ca^{2+}	0.96	0.24	100.5 ± 2.9	3.4 ± 0.3
	Pb^{2+}	1.11	0.18	–	–
	$Ca^{2+} + Pb^{2+}$	1.12	0.17	–	–
N53I	Apo	0.89	–	18.1 ± 0.8	1.6 ± 0.1
	Ca^{2+}	0.95	0.18	35.4 ± 2.1	1.2 ± 0.1
	Pb^{2+}	1.12	0.14	–	–
	$Ca^{2+} + Pb^{2+}$	1.12	0.10	–	–
N97S	Apo	0.91	–	17.3 ± 0.7	2.3 ± 0.2
	Ca^{2+}	0.96	0.19	25.5 ± 0.1	1.3 ± 0.1
	Pb^{2+}	1.15	0.12	–	–
	$Ca^{2+} + Pb^{2+}$	1.13	0.11	–	–
E104A	Apo	0.90	–	17.1 ± 0.8	1.6 ± 0.1
	Ca^{2+}	0.94	0.11	23.2 ± 0.1	1.1 ± 0.1
	Pb^{2+}	1.13	0.06	–	–
	$Ca^{2+} + Pb^{2+}$	1.12	0.04	–	–
F141L	Apo	0.87	–	44.9 ± 15.1	0.9 ± 0.2
	Ca^{2+}	0.91	0.01	69.2 ± 3.8	3.1 ± 0.4
	Pb^{2+}	1.12	0.06	–	–
	$Ca^{2+} + Pb^{2+}$	1.11	0.04	–	–

[a] ratio between CD signal at 222 and 208 nm.
[b] Relative variation in ellipticity calculated as $(\theta_{222}^{ion} - \theta_{222}^{apo})/\theta_{222}^{apo}$.
[c] Pb^{2+} concentration at which the observed conformational transition affecting secondary structure is half-maximal.

2.5. Molecular modeling

Molecular models for: i) Ca^{2+}-loaded, ii) Pb^{2+}-loaded, and iii) the intermediate $Pb^{2+}+Ca^{2+}$ state (Pb^{2+} ions bound to EF1 and EF2, Ca^{2+}-ions bound to EF3 and EF4, Fig. 1) of CaM WT and arrhythmia-associated variants were generated within the BioLuminate framework provided by Schroedinger's Maestro chemical simulation suite.

The three-dimensional structure of Ca^{2+}-loaded WT CaM was modeled using the experimentally solved crystallographic structure as a template (PDB entry 1CLL, 1.7 Å resolution [28]). The structure of the Pb^{2+}-loaded form, on the other hand, was modeled using the crystallographic structure as a template (PDB entry 2V01, 2.15 Å resolution [49]) after removing all opportunistically bound ions, thus retaining only Pb^{2+}-ions canonically bound to the four EF-hand motifs. Finally, the intermediate structure was built upon superimposition of the coordinates of Cα atoms of Ca^{2+}-loaded and the Pb^{2+}-loaded forms (Root-Mean Square Deviation, RMSD = 0.58 Å) and by fusing the N-terminal part of the Pb^{2+}-loaded state (residues 5–80) with the C-terminal part of the Ca^{2+}-loaded state (residues 81–147), due to the 8-fold higher affinity for Pb^{2+} exhibited by the N-lobe compared to that exhibited for Ca^{2+} [33].

All three states were subjected to BioLuminate's "Protein preparation" protocol as previously described [50], briefly summarized as: assignment of bond orders (including 0-order bonds involving Ca^{2+} and Pb^{2+}-ions) as provided by the Chemical Components Dictionary database; addition of hydrogens; sampling of water molecules; assignment of the protonation state at pH 7.5 using PROPKA; H-bond optimization and heavy atom minimization (RMSD <0.3 Å). Arrhythmia-causing mutations N53I, N97S, E104A and F141L were generate by the "Mutate residue" tool implemented in BioLuminate, upon selection of the highest-scored non-clashing rotamer.

2.6. Molecular dynamics simulations

CaM variants in their Ca^{2+}-loaded, Pb^{2+}-loaded, and intermediate states underwent 1 μs all-atom molecular dynamics (MD) simulations performed with GROMACS 2020.6 [53] simulation suite and CHARMM36m force field [54]. Proteins were then surrounded by a dodecahedral water box with 1.2 nm distance between protein atoms and the edges of the box, neutralized with 150 mM KCl (total system size ~55,000 atoms), subjected to a two-step energy minimization using steepest descent and conjugate gradient algorithms, and equilibrated for 2 ns in NVT and for 2 ns in NPT ensemble, as previously detailed [55]. Finally, each system was simulated for 1 μs in NPT ensemble, where temperature and pressure were set to 37 °C and 1 atm, respectively.

2.7. Analysis of molecular dynamics trajectories

To assess the effects of pathological mutations and different metal cations on the flexibility of the backbone of CaM, the Root-Mean Square Fluctuation of Cα (RMSF), representing the time-averaged deviation of the position of each Cα with respect to its average position, was calculated for each variant/state combination by the "gmx rmsf" function provided by GROMACS.

Analogously, the time-evolution over 1 μs of the radius of gyration of each CaM variant in the three ion-bound states was calculated by "gmx gyrate" function provided by GROMACS. To evaluate potential conformational transitions responsible for remarkable changes in the radius of gyration, a single structure was extracted from the trajectory for each ns of simulation time. The representative conformation for each ns of the trajectory was identified as the centroid of the cluster, that is the structure with the lowest Cα-RMSD with respect to all other conformations, thus yielding trajectories constituted by 1000 frames. Then, each trajectory was clustered using the single linkage method by setting 2.5 Å as cutoff for the Cα-RMSD, and the centroid of the two most populated clusters comprising at least 100 members (if present, see Table ST1) were considered as the representative conformation(s) of each state. The solvent-accessibility of Ca^{2+} and Pb^{2+} ions was monitored over the 1 μs trajectory to evaluate the potential dissociation of ions from the binding loops of the four EF-hand motifs using GROMACS function "gmx sasa".

Data referring to the time evolution of the cations' solvent accessibility and of the protein radius of gyration were smoothed by calculating the running average over a 5-ns time window, plotted results refer to the average ± standard deviation of the 5-ns time window.

2.8. Fluorescence spectroscopy

The apparent affinity (K_d) of CaM variants for RyR2 peptide was measured by fluorescence spectroscopy titrations, performed using a Jasco FP750 spectrofluorometer as described in [56], by taking advantage of the presence of the sole Trp in RyR2 peptide. Briefly, 1 μM RyR2 peptide was incubated with increasing concentration of CaM (0–4 μM) variants in the presence of 80 μM Ca^{2+} and after the addition of 80 μM Pb^{2+}. Each titration was performed in triplicate, emission spectra were collected between 300 and 400 nm following excitation at $\lambda^{ex} = 295$ nm. Data was fitted to a one-site saturation ligand binding function ($fb = \frac{fb_{max}*x}{K_d+x}$), where fb is the peptide's fraction bound to CaM, fb_{max} is the maximum degree of saturation (theoretically 1), K_d is CaM affinity for the peptide, and x is the concentration of CaM, as previously described [57]. All spectra were collected at 37 °C using a thermostat system.

8-Anilinonaphthalene-1-sulfonic acid (ANS) fluorescence was used to probe the changes in hydrophobicity of CaM variants upon binding of Ca^{2+} and Pb^{2+}. Fluorescence emission spectra of 4 μM CaM were collected between 445 and 650 nm upon excitation at 380 nm in the presence of 30 μM ANS + 80 μM EDTA and after sequential additions of 160 μM Ca^{2+} (~80 μM free Ca^{2+}) and 80 μM Pb^{2+}. Spectra were collected at 37 °C after setting excitation and emission band width at 5

nm, fast response, and data pitch at 1 nm. Reported spectra represent the average of three accumulations after subtraction of the spectrum of the sole buffer (20 mM TRIS pH 7.5, 150 mM KCl), which was considered as blank.
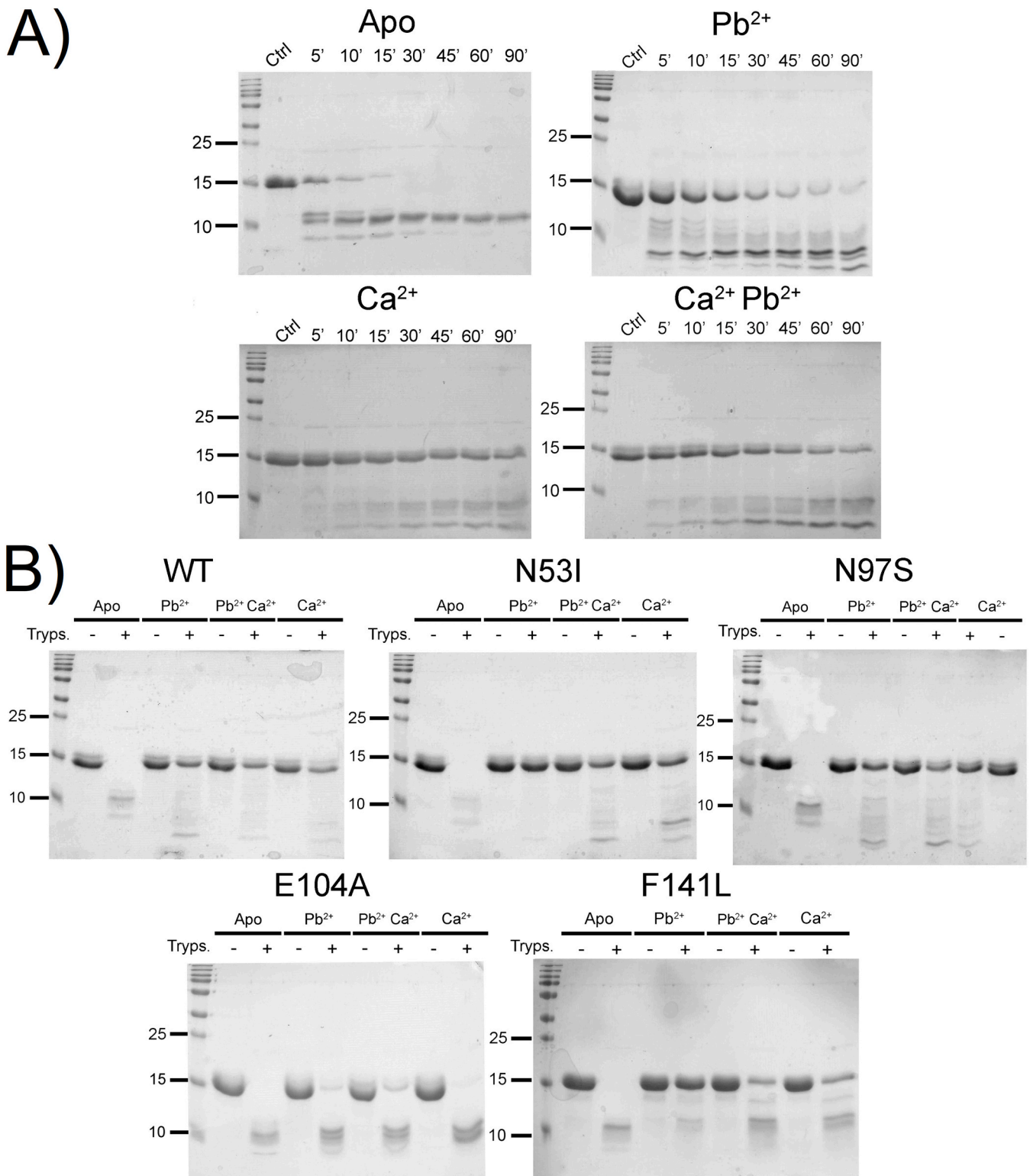
Fig. 2. Limited proteolysis. A) Time scan of limited proteolysis of WT CaM performed at 25 °C by incubating 26.6 μM CaM with 0.4 μM trypsin (ratio 1:66) in four conditions: apo (200 μM EDTA), Pb^{2+} (100 μM EDTA + 200 μM Pb^{2+}, corresponding to free Pb^{2+} ~100 μM), Ca^{2+} (500 μM), and co-presence of Pb^{2+} and Ca^{2+} (100 μM Pb^{2+} + 500 μM Ca^{2+}). B) Limited proteolysis profiles of WT CaM and mutant forms after 10 min incubation at 37 °C using the same trypsin and cations concentrations as in (A).

3. Results and discussion

3.1. Effects of Ca²⁺ and Pb²⁺-binding on the trypsin susceptibility of CaM variants

The accessibility of basic residues of CaM to the proteolytic enzyme trypsin was employed to evaluate at low resolution the conformational changes upon Ca^{2+} and Pb^{2+} binding. The time-resolved proteolytic pattern exhibited by WT CaM at 25 °C in the absence and in the presence of ions (Fig. 2A) indicated that in all tested conditions a 10-min digestion allows a clear identification of the bands of both the proteolytic fragments and the residual undigested protein. Limited proteolysis experiments suggested that the apo form (Fig. 2A, top left panel) is cleaved in two distinct fragments with a molecular mass >10 kDa and an additional peptide at a slightly lower molecular weight. Interestingly, Pb^{2+}-bound CaM was found to be less prone to tryptic digestion than its apo form (Fig. 2A, top right panel), as shown by the persistent presence of the band representing the undigested protein. Moreover, Pb^{2+}-bound CaM displayed a higher number of proteolytic fragments, most of which at a smaller molecular weight compared to the apo form, indicative of a different susceptibility to trypsin. Ca^{2+}-bound CaM, on the other hand, showed a more intense band at the theoretical molecular weight of full-length CaM (~17 kDa) and several faint bands corresponding to the proteolytic fragments, thus suggesting that this was the most stable form. Finally, in the co-presence of Ca^{2+} and Pb^{2+}, CaM exhibited a proteolytic pattern similar to that of the Ca^{2+}-bound form, although the intensity of the most abundant fragment below 10 kDa was more pronounced, with a behavior resembling that of the Pb^{2+}-bound form (Fig. 2A). In addition, the cleavage efficiency of trypsin in the presence of both ions was halfway between the Pb^{2+}- and the Ca^{2+}-bound forms, suggesting a potential additive effect of the two ions (Fig. 2A) on the exposure of CaM to trypsin. A proteolytic time of 10 min was found to be optimal for proper resolution of the digested bands, therefore limited proteolysis was performed for all CaM variants at 25 °C (Fig. S1) and 37 °C (Fig. 2B) to evaluate the temperature effect on trypsin accessibility and to reproduce physiological conditions. The proteolytic patterns showed by all variants at the two different temperatures were substantially identical (compare Fig. 2B and Fig. S1), although a lower amount of undigested protein was present at 37 °C, which was somehow expected, as the higher temperature increases CaM flexibility and is closer to the optimum temperature for trypsin's enzymatic activity.

Arrhythmia-associated CaM variants showed mutation-specific proteolytic patterns. The N53I variant showed overall a WT-like proteolytic pattern, exception made for the Pb^{2+}-bound form, which was found to be more stable than the WT (Fig. 2B). Moreover, the persistence of the band corresponding to the full-length protein under all cation-loading conditions tested suggested that the N53I variant was the least susceptible to trypsin among the four arrhythmia-associated variants.

In line with the N53I variant, the N97S variant showed a fragment distribution similar to that of the WT under all ion-loading conditions, at odds with E104A and F141L, which showed a peculiar proteolytic pattern in their ion-bound forms, characterized by two predominant fragments at ~10 kDa similar to those present in their apo forms. Nevertheless, the cleavage efficiency of E104A and F141L variants was found to depend on the specific ion-loading state. Noteworthy, in the presence of the E104A substitution, the band corresponding to the undigested protein was hardly detectable and only in the presence of Pb^{2+}, thus implying that this variant was the least stable among all tested variants. In summary, arrhythmia-associated mutations perturbed the exposure to trypsin with a WT-like (N53I and N97S) or a different (E104A, F141L) pattern. On the other hand, although Pb^{2+} was found to decrease trypsin accessibility of all tested variants compared to the apo form, such behavior was strictly mutation dependent, as N53I, E104A, and F141L were found to be less susceptible to proteolytic cleavage compared to their Ca^{2+}-bound forms, at odds with the WT or the N97S variants.

3.2. Effects of Ca²⁺ and Pb²⁺-binding on the secondary structure of WT CaM

To dissect the conformational change associated with ion binding to CaM we used CD spectroscopy, which provides information on protein secondary structure by exploiting the optical activity of the peptide bond in the far-UV (200–250 nm, Fig. 3).

As expected by a nearly all α-helical protein, the far-UV CD spectrum of WT CaM (Fig. 3A) displayed the typical minima at 208 and 222 nm, which can be conveniently employed to describe the shape of the spectrum and monitor secondary structure rearrangements. Indeed, Ca^{2+}- binding to WT CaM resulted in a significant increase in ellipticity at 222 nm ($\Delta\theta_{222}/\theta_{222} = 0.24$, Table 1) accompanied by an increase in the $\theta_{222}/\theta_{208}$ ratio (0.90 vs 0.96, Table 1), indicative of a major variation in protein secondary structure (Fig. 3A). Pb^{2+}-binding to WT CaM also triggered a major conformational rearrangement, as shown by the $\theta_{222}/\theta_{208}$ reaching 1.11 (Table 1), and by the $\Delta\theta_{222}/\theta_{222} = 0.18$ (Table 1). Interestingly, in the presence of equimolar concentrations of Pb^{2+} and Ca^{2+} both spectral descriptors were found to be almost identical to those exhibited by the Pb^{2+}-bound form ($\theta_{222}/\theta_{208} = 1.12$ vs 1.11 and $\Delta\theta_{222}/\theta_{222} = 0.17$ vs 0.18, Table 1) regardless of the order of ion additions. Since $\theta_{222}/\theta_{208}$ values exceeding 1 have been shown to be typical of interacting α-helices [58] forming coiled-coil assemblies [59,60], our data suggest that Pb^{2+} can displace at least some Ca^{2+}-ions bound to CaM and trigger the acquisition of a coiled-coil conformation. On the contrary, Ca^{2+}-ions are not capable of replacing Pb^{2+}-ions bound to WT CaM, which becomes "locked" in the coiled-coil secondary structure conformation.

Overall, our results suggest that, when it comes to CaM secondary structure, Ca^{2+} and Pb^{2+} may exert an additive rather than synergistic effect, in line with limited proteolysis experiments, and further confirm that Pb^{2+} may displace Ca^{2+} ions (but not the other way round) from the binding loops.

Moreover, it is worth noting that the Pb^{2+}-bound and Ca^{2+}-bound forms exhibited different secondary structures, as the coiled-coil conformation was present only in the presence of Pb^{2+}, which may be ascribable to a rearrangement of the central linker helix.

3.3. Ca²⁺ modulates the Pb²⁺-induced changes in secondary structure of CaM in a mutation-dependent fashion

Since far-UV CD spectra excluded major differences in the secondary structure of WT CaM upon Pb^{2+}-binding regardless of the presence of Ca^{2+}, we asked whether the presence of arrhythmia-associated mutations could affect the observed changes in secondary structure induced by Pb^{2+}. We thus monitored the spectral descriptor $\theta_{222}/\theta_{208}$ as a function of $[Pb^{2+}]$ up to 320 μM.

Interestingly, in the absence of Ca^{2+}, the secondary structure rearrangement of all five variants upon Pb^{2+}-binding followed a sigmoidal distribution (Fig. 4), with Hill coefficients ranging between 0.9 and 2.3 (Table 1), thus suggesting that the process occurred with a different mechanism for all variants, from sequential to cooperative, with N97S displaying the highest cooperativity. The EC_{50} of all CaM variants was found to be in the micromolar range, with all arrhythmia-associated mutants displaying significantly lower Pb^{2+}-concentrations required for the half-maximal transition to the coiled-coil secondary structure (Table 1, *p*-value <0.03 for all variants) compared to the WT. Specifically, variants affecting EF2 (N53I) and EF3 (N97S and E104A) exhibited comparable EC_{50} values (18.1 ± 0.8 μM, 17.3 ± 0.7 μM, and 17.1 ± 0.8 μM, respectively, Table 1) which were >3-fold lower with respect to the WT (69.8 ± 21.0 μM). On the other hand, the F141L variant affecting EF4 showed a 1.5-fold decrease in EC_{50} (44.9 ± 15.1 μM vs 69.8 ± 21.0 μM) compared to the WT, thus implying a milder molecular phenotype.

Titrations in the presence of saturating Ca^{2+} also followed a sigmoidal trend (Fig. 4), suggesting a cooperative structural
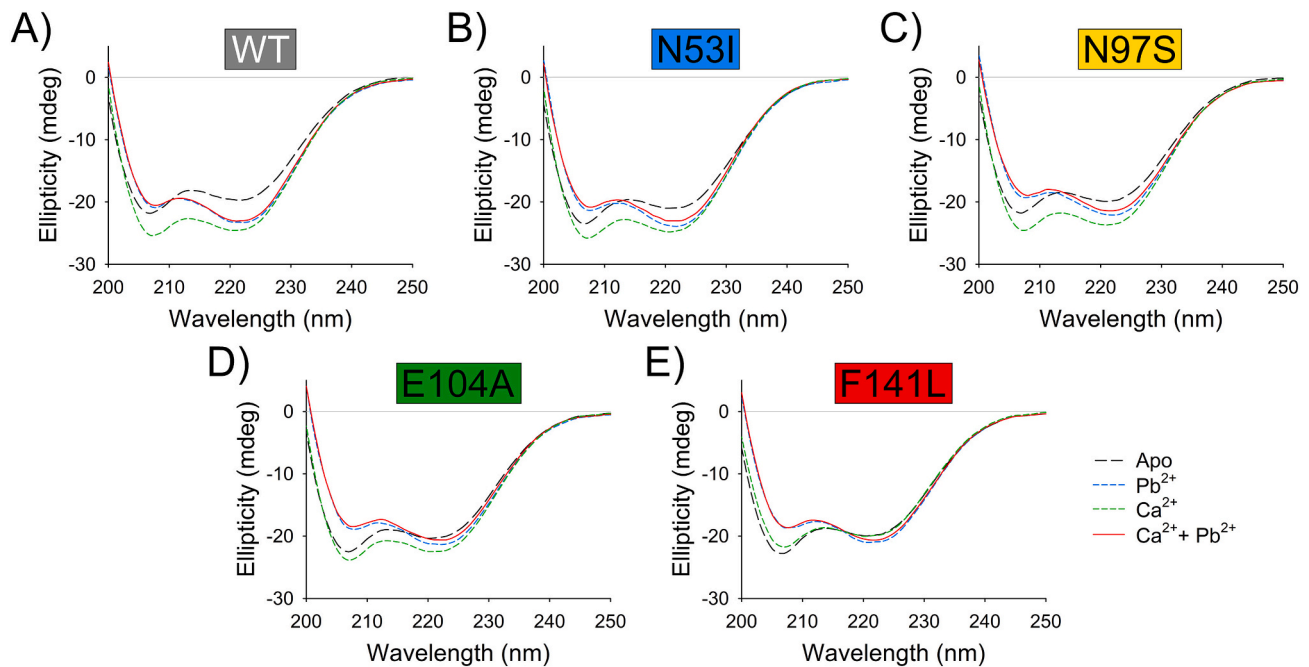
Fig. 3. Effects of Ca^{2+} and Pb^{2+} on the secondary structure of CaM variants. Far-UV CD spectra of 10 μM CaM A) WT, B) N53I, C) N97S, D) E104A, E) F141L variants in the absence of ions (apo, black long-dashed line) and in the presence of 200 μM Ca^{2+} (green dashed line), 200 μM Pb^{2+} (blue dashed line) or 200 μM Pb^{2+} and 200 μM Ca^{2+} (red solid line).
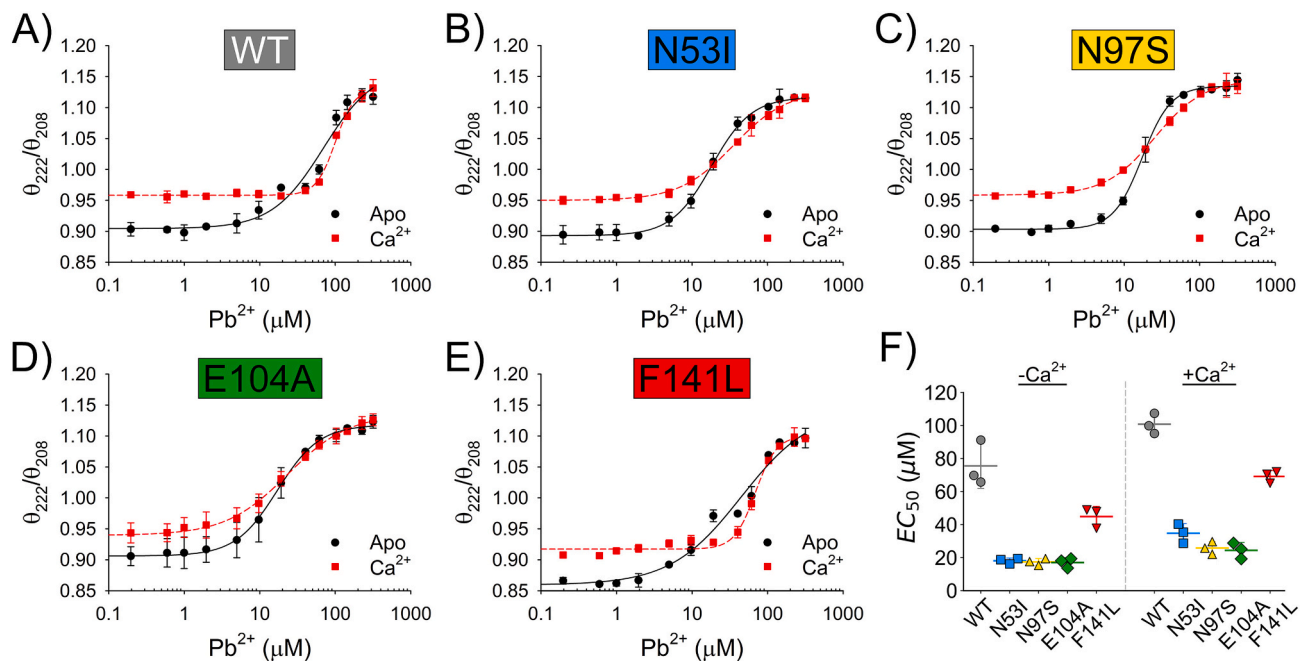
Fig. 4. Conformational transition of CaM variants induced by Pb^{2+}: far-UV CD titrations. Pb^{2+}-titrations (0–320 μM range) of 10 μM CaM variants A) WT, B) N53I, C) N97S, D) E104A, E) F141L in the absence (apo, black circles) and in the presence of 200 μM Ca^{2+} (red squares) performed by monitoring the ratio between the ellipticity at 222 and 208 nm. Titrations were performed in triplicate, graphs represent the average and the standard deviation of the observable for each titration point, together with the respective fitting to a four-parameter Hill sigmoid (apo, black solid line; Ca^{2+}, red dashed line). F) Scatter plot of the individual EC_{50} values (calculated as detailed in the results section) obtained for each titration performed on CaM WT (grey), N53I (blue), N97S (yellow), E104A (green), F141L (red), their average and standard deviation (see Table 1). The statistical significance of the differences in EC_{50} values was assessed by two-tailed t-tests; p-values <0.03 in all comparisons with the WT, p-values <0.043 in all comparisons between apo and Ca^{2+}-loaded forms, except for E104A variant (p-value = 0.086).

rearrangement towards a coiled-coil assembly for most tested variants. In line with the results obtained in the absence of Ca^{2+}, the EC_{50} measured for all arrhythmia-associated variants was found to be significantly lower than the WT (p-value <0.002 for all variants). In

detail, such decrease in EC_{50} was found to be mutation-dependent, with the N97S and E104A substitutions exhibiting a 4-fold decrease (25.5 ± 0.1 μM and 23.2 ± 0.1 μM, respectively vs 100.5 ± 2.9 μM, Table 1), the largest among all tested variants, and N53I showing a ~3-fold reduction

(35.4 ± 2.1 μM, Table 1). Finally, the F141L variant displayed the smallest difference in EC_{50} with respect to the WT (69.2 ± 3.8 μM vs 100.5 ± 2.9 μM, Table 1) among all tested variants, which corresponds to a ~1.4 fold lower Pb^{2+}-concentration.

Noteworthy, apart from the E104A mutant, whose differences in EC_{50} in the presence and in the absence of Ca^{2+} (23.2 ± 0.1 μM vs 17.1 ± 0.8 μM, Table 1) just fell short of statistical significance (*p*-value = 0.086), all other variants exhibited significantly higher EC_{50} in the presence of Ca^{2+} (*p*-value <0.043 for all other variants). Overall, all arrhythmia-associated variants were more susceptible to Pb^{2+} than WT CaM, as the conformational transition towards the coiled-coil conformation occurred at lower Pb^{2+}, regardless of the presence of Ca^{2+}.

As to the specific conformation of each variant, the analysis of the spectral shape indicated that N53I acquired a WT-like secondary structure (Fig. 3B), with almost identical $\theta_{222}/\theta_{208}$ values under all ion-loading conditions (differences with the WT <0.01, Table 1), although the increase in ellipticity upon ion binding ($\Delta\theta_{222}/\theta_{222}$) was overall smaller than that exhibited by the WT. The spectra of N97S variant (Fig. 3C) displayed a WT-like behavior in terms of $\theta_{222}/\theta_{208}$ values under all states (differences with the WT <0.01, Table 1), with the only exception being the Pb^{2+}-bound form, which showed a more pronounced $\theta_{222}/\theta_{208}$ with respect to the WT (1.15 vs 1.11, Table 1). On the other hand, the relative increase in ellipticity upon ion binding was overall lower than that exhibited by the WT, particularly in the presence of Pb^{2+} (0.12 vs 0.18, Table 1), and of both Ca^{2+} and Pb^{2+} (0.11 vs 0.17, Table 1).

As to the E104A variant, the most relevant differences in spectral shape (Fig. 3D) with respect to the WT were found upon binding to a single ion species ($\theta_{222}/\theta_{208}^{Ca}$ = 0.94 vs 0.96 and $\theta_{222}/\theta_{208}^{Pb}$ = 1.13 vs 1.11, Table 1), possibly indicative of a slight alteration in secondary structure due to defective Ca^{2+}-coordination in EF3. Strikingly, Ca^{2+}-binding to E104A variant resulted in a 2-fold smaller increase in ellipticity at 222 nm compared to the WT ($\Delta\theta_{222}/\theta_{222}$ = 0.11 vs 0.24), while Pb^{2+}-binding/Ca^{2+}-displacement further reduced the $\Delta\theta_{222}/\theta_{222}$ associated with physiological ion binding to 0.06 and 0.04, respectively (Table 1).

Finally, the spectra of the F141L variant (Fig. 3E) displayed a lower $\theta_{222}/\theta_{208}$ both in the absence (0.87 vs 0.90, Table 1) and in the presence of Ca^{2+} (0.91 vs 0.96, Table 1), whereas no differences were detected when Pb^{2+} was present (Fig. 3E and Table 1). Similar to the E104A substitution, F141L exhibited smaller $\Delta\theta_{222}/\theta_{222}$ values upon ion binding with respect to the WT, ranging from 3-fold in the presence of Pb^{2+} (0.06 vs 0.18, Table 1) to 24-fold in the presence of Ca^{2+} (0.01 vs 0.24, Table 1). Overall, our results point towards the role of the EF3 and EF4 motifs (belonging to the C-terminal domain) in shaping the correct conformational transition. These results are substantially in line with previous observations by Martin and Bayley [61] on the C-terminal domain of CaM, which showed a higher increase in ellipticity upon Ca^{2+}-binding compared to the N-terminal lobe, associated with an increase in protein compactness or α-helical content.

3.4. Investigation of CaM variants hydrophobicity via ANS fluorescence

Ca^{2+}-binding to CaM is known to induce an increased exposure of its hydrophobic surface patches, resulting in a versatile protein capable of interacting with a plethora of molecular targets. Thus, we assessed the transition from apo to Ca^{2+}- and Ca^{2+}/Pb^{2+}-bound states of CaM variants using the fluorescent probe ANS (Fig. S2), which binds the hydrophobic patches of the protein surface, by monitoring: i) the change in the wavelength of maximal ANS fluorescence emission of the proteins under different cation-loading conditions ($\Delta\lambda$, Table 2), and ii) the ratio between their intensities (I_{max}/I_{max}^{ANS}, Table 2). The apo form of all tested CaM variants exhibited fluorescence emission profiles (Fig. S2, black dashed lines) almost undistinguishable from those of the probe in the absence of proteins (Fig. S2, grey solid lines), as shown by the minor differences found in both $\Delta\lambda$ and I_{max}/I_{max}^{ANS} ratio (Table 2), ranging from 0 to 4 nm and 1.0 to 1.2 respectively. As expected, Ca^{2+}-binding resulted

Table 2
Results from fluorescence measurements.

Variant	State	$\Delta\lambda$ (nm)[a]	I_{max}/I_{max}^{ANS}[b]	K_d (nM)[c]
WT	Apo	2	1.06	–
	Ca^{2+}	29	4.12	331.0 ± 8.8
	$Ca^{2+} + Pb^{2+}$	33	4.80	171.7 ± 19.5
N53I	Apo	2	1.16	–
	Ca^{2+}	28	4.34	339.0 ± 47.3
	$Ca^{2+} + Pb^{2+}$	31	4.86	350.7 ± 73.6
N97S	Apo	0	1.11	–
	Ca^{2+}	30	5.51	333.5 ± 49.5
	$Ca^{2+} + Pb^{2+}$	34	5.67	460.1 ± 354.5
E104A	Apo	2	1.26	–
	Ca^{2+}	40	10.68	231.0 ± 5.5
	$Ca^{2+} + Pb^{2+}$	39	11.31	157.9 ± 85.3
F141L	Apo	4	1.06	–
	Ca^{2+}	36	6.11	225.1 ± 51.4
	$Ca^{2+} + Pb^{2+}$	36	6.35	222.7 ± 28.9

[a] Variation of the wavelength at which the intensity of fluorescence emission of ANS (λ^{ex} = 380 nm) was maximal, calculated as $\lambda_{condition}$ - λ_{ANS}.

[b] Ratio between the maximal intensity of fluorescence emission of ANS (λ^{ex} = 380 nm) in the presence and in the absence of CaM variants under different cation-loading conditions.

[c] Dissociation constant of the CaM-RyR2 complex estimated by monitoring the intrinsic fluorescence emission of RyR2 peptide upon excitation at 295 nm.

in a significant blue shift for all variants (Fig. S2, red solid lines), with $\Delta\lambda$ values spanning between 29 nm and 40 nm (Table 2), accompanied by an increased maximal fluorescence emission (Table 2). The addition of Pb^{2+} on top of Ca^{2+} (blue dashed lines) resulted in a further, less pronounced blue shift (<4 nm), together with a slight increase in intensity for all tested variants. Interestingly, such relative fluorescence increase upon Ca^{2+}-displacement/Pb^{2+}-binding was more pronounced for the WT compared to the arrhythmia-associated variants, particularly for those located in the C-terminal domain, namely N97S, E104A, and F141L. Notably, E104A variant exhibited the largest variations in hydrophobicity upon ion binding among all tested variants, suggesting local rearrangements of hydrophobic residues surrounding the ion-binding loop of EF3, which is not surprising considering that the bidentate-ion coordinating residue glutamate 104 is replaced by an hydrophobic alanine in the arrhythmia-associated variant. Overall, our results indicate that while Ca^{2+}-binding largely increased the hydrophobicity of all CaM variants, the addition of Pb^{2+} on Ca^{2+}-bound CaM resulted in a minor increase of their hydrophobicity, suggesting that replacement of Ca^{2+} by Pb^{2+} does not lead to dramatic conformational changes, in line with previous findings [28,49]. Concerning the effects of the mutations on CaM hydrophobicity, all four tested variants exhibited a WT-like behavior in terms of increased hydrophobicity upon Ca^{2+}-binding followed by a further smaller increase upon Pb^{2+} addition. Nevertheless, CaM variants affecting the C-terminal lobe, namely N97S, E104A, and F141L were found to be more hydrophobic than N53I, the only mutation located in the N-terminal lobe.

3.5. Cation-specific effects on the structural properties of CaM variants monitored by molecular dynamics simulations

Extensive and exhaustive Molecular Dynamics (MD) simulations provide atomistic insights on the molecular properties of CaM variants upon ion binding [50,51]. Therefore, we ran 1 μs MD simulations for each CaM variant in their Ca^{2+}-loaded, Pb^{2+}-loaded, and intermediate state (Pb^{2+}-ions bound to EF1 and EF2, Ca^{2+}-ions bound to EF3 and EF4; see Fig. 1). For each trajectory, we calculated the Root-Mean Square Fluctuation (RMSF) of Cα, that is the RMSD averaged over the simulated timeframe calculated with respect to the average structure, to investigate the combined effects of ions and pathological variants on protein flexibility (Fig. 5). The comparison of the Ca^{2+}-loaded form of CaM variants highlighted that the N53I, and more prominently, the E104A variant were overall more flexible than the WT, particularly in the C-
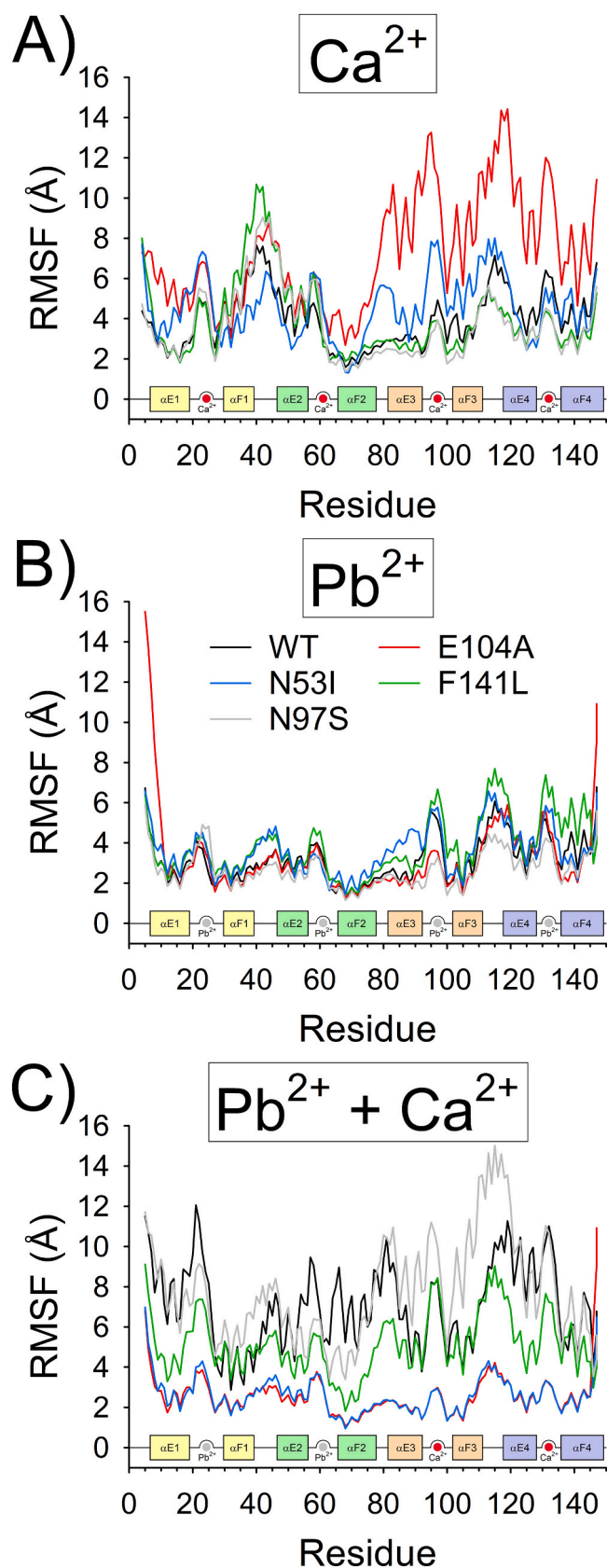
Fig. 5. Effects of Pb^{2+} and Ca^{2+} binding on the backbone flexibility of CaM variants. Root-Mean Square Fluctuation (RMSF) calculated on Cα of A) the Ca^{2+}-loaded, B) Pb^{2+}-loaded, and C) intermediate state (Pb^{2+}-ions bound in EF1 and EF2, Ca^{2+}-ions bound in EF3 and EF4) of CaM variants WT (black), N53I (blue), N97S (grey), E104A (red), and F141L (green). Inset show a schematic representation of the secondary structure of the protein (colored according to Fig. 1), the position of each EF-hand motif and the ion bound in each condition, with Ca^{2+} ions represented as red circles and Pb^{2+} ions by grey circles.

terminal domain (Fig. 5A). This was not surprising for the E104A mutation, as the substitution affects the EF3 Ca^{2+}-binding loop; however, this is not the case for the N53I substitution, which is located in the EF2 motif, thus, our results suggest an allosteric effect of the N53I mutation on CaM flexibility, in line with previous results from NMR relaxation dispersion experiments [62]. In contrast, N97S and F141L substitutions, affecting EF3 and EF4, respectively, exhibited highly similar RMSF profiles throughout the structure, with a slightly higher flexibility in the N-terminal domain and a higher structural rigidity in the C-terminal domain compared to the WT.

Interestingly, the Pb^{2+}-loaded form of CaM variants, that is with four Pb^{2+}-ions bound only to the canonical EF-hand motifs, displayed overall smaller differences compared to the WT, and in general were less flexible than their Ca^{2+}-loaded counterparts (Fig. 5B). Concerning the putative intermediate state (Fig. 5C), both N53I and E104A mutations exhibited a strikingly high structural rigidity in both domains, with an almost complete overlap of the RMSF profiles. This is very surprising, as the mutations are located in two different lobes, namely the N-terminal (N53I) and the C-terminal (E104A) lobe (Fig. 1). The concomitant binding of Pb^{2+} to the N-terminal domain and of Ca^{2+} to the C-terminal lobe is evidently creating long range connections that stabilize the structure of CaM in a mutation-dependent way. On the contrary, WT CaM was found to be extremely flexible along the entire structure, pointing towards an equilibrium between different conformations. A similar conclusion could be drawn by analyzing RMSF profiles for N97S and F141L variants, although the former displayed even higher flexibility in the C-terminal domain, while the latter was slightly more rigid than the WT.

To investigate the molecular consequences of changes in protein flexibility due to the combined effect of amino acid replacement and different ion-loading states, we monitored for each combination the radius of gyration of the proteins (Fig. 6), which represents a physical quantity proportional to protein compactness, and grouped them in homogeneous clusters along the 1 μs MD trajectory.

As suggested by the RMSF profiles, WT CaM exhibited mainly a single ensemble of conformations in both the Ca^{2+}-loaded and Pb^{2+}-loaded states, accounting for >97.7 % of the simulation time (Table ST1) in both cases. In line with X-ray crystallographic data [28,49], their representative conformations were similar, with a Cα-RMSD of 3.7 Å. At odds with the ion-loaded forms, the intermediate state of WT CaM displayed a major decrease in the radius of gyration at ~550 ns, indicative of a conformational switch between a dumbbell-like open structure (37 % of the trajectory, Table ST1) and a closed structure (43.4 % of the simulation time, Table ST1). The visual inspection of the two structures indicated that such structural transition was due to the break of linker helix connecting the N- and C-terminal domain, which allowed the two domains to come closer to each other (Fig. 6A, inset). The time evolution of the radius of gyration of the N53I variant pointed towards a single conformational ensemble for both the Pb^{2+}-loaded and intermediate states visited for >96.2 % of the simulation (Table ST1), compatible with the open structure (Fig. 6B). Interestingly, while the structure of Pb^{2+}-loaded N53I variant was different from the WT (Cα-RMSD = 5.0 Å), the intermediate state was comparable to the open conformation of the WT (Cα-RMSD = 1.2 Å). In the Ca^{2+}-loaded form, though, the mutation caused a contraction of the structure, which allowed to identify two main conformational basins representing 72.1 % and 23.7 % of the
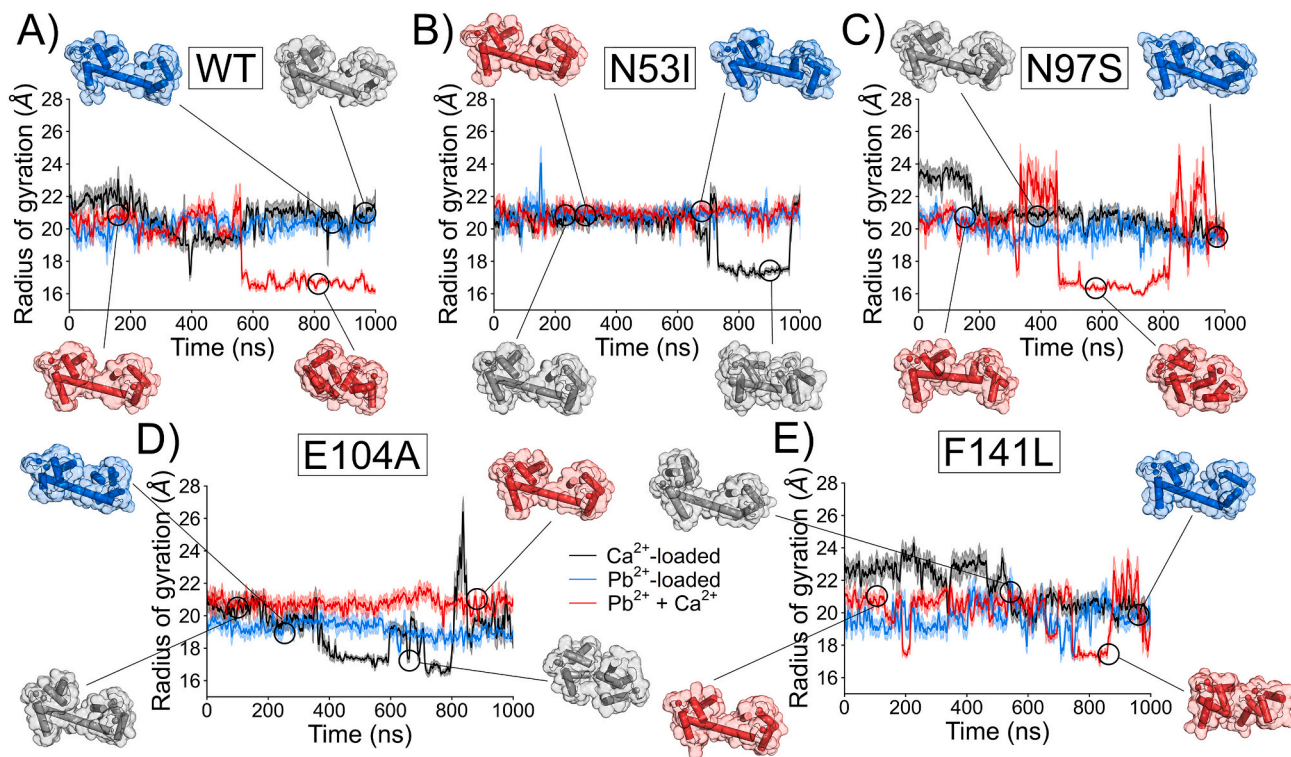
Fig. 6. Time-dependence of the radius of gyration of CaM variants upon binding to Ca^{2+} and/or Pb^{2+}. Time evolution over 1 μs of the radius of gyration of CaM variants A) WT, B) N53I, C) N97S, D) E104A, E) F141L in their Ca^{2+}-loaded (black), Pb^{2+}-loaded (blue), and intermediate states (Pb^{2+}-ions bound in EF1 and EF2, Ca^{2+}-ions bound in EF3 and EF4; red). Each point represents the average ± standard deviation of the values smoothed over a 5-ns window as described in the methods section. Insets show the most representative conformation(s) of the respective variant/state combination identified as detailed in the methods section.

trajectory. Noteworthy, and at odds with the intermediate state of the WT, the closed structure of Ca^{2+}-loaded N53I did not exhibit any break in the linker helix (Fig. 6B, inset). Nevertheless, the reorientation of the Ca^{2+}-binding loops of EF2 and EF3, as well as the entire EF1 and EF4 motifs, was the driving force leading to the closed structure. Similarly to the WT, the N97S substitution did not show any major structural rearrangement throughout the simulation of either the Ca^{2+}-loaded or the Pb^{2+}-loaded states (Fig. 6C), as the respective open conformation was present in 99.5 % of the trajectory (Table ST1), and were relatively similar to each other (Cα-RMSD = 3.6 Å). The intermediate state of N97S, instead, exhibited larger fluctuations in terms of radius of gyration, allowing the identification of two predominantly visited structural clusters, namely the open (29.2 % of the simulation) and the closed conformation (35.7 % of the trajectory). Again, and similarly to the WT, in the closed conformation the linker helix was broken, allowing the N- and C-terminal domains to directly interact with each other (Fig. 6C, inset). Finally, it is worth noting that the intermediate state of N97S acquired a much larger number of different conformations during the simulation, although such different conformations were significantly less persistent, as they represented <10 % of the trajectory.

The Ca^{2+}-loaded form of E104A variant exhibited a peculiar behavior compared to all other variants, as its radius of gyration was found to vary between ~16 Å and ~26 Å (Fig. 6D), in line with the high flexibility shown in the RMSF profile. Indeed, the cluster analysis of the trajectory identified the two main ensembles corresponding to the open and closed conformation, acquired for 33 % and 29.5 % of the trajectory, respectively. Similarly to the intermediate form of N97S variant, the Ca^{2+}-loaded E104A mutant transiently visited a large number of conformational basins, indicative again of an enhanced structural plasticity, and its closed conformation displayed the same break of the linker helix (Fig. 6D, inset). As to the Pb^{2+}-loaded and intermediate states, the E104A variant acquired predominantly the open conformation during both simulations, as their representative structural ensembles included

98.9 % and 99.3 % of the frames of the trajectory (Table ST1), although with a different relative orientation of the N- and C-terminal EF-hand motifs.

The last of the tested variants, namely F141L, displayed a WT-like behavior in terms of conformational basins visited by each simulation (Fig. 6E). Indeed, the conformations explored by both the Ca^{2+}-loaded and the Pb^{2+}-loaded forms of F141L could be grouped in a single cluster corresponding to their open structure (Fig. 6E, inset), which represented 95.5 % and 99.1 % of the trajectory, respectively. On the contrary, F141L in its intermediate state exhibited again a structural rearrangement during the simulation from the open conformation, present in the first 72.5 % of the trajectory, to the closed conformation, reached during the last 151 ns of the simulation. Interestingly, the closed intermediate conformation of F141L variant showed the same rupture of the linker helix seen in N97S and WT CaM, though accompanied by a peculiar relative orientation of the N- and C-terminal domains where the helices constituting EF1 and EF2 had the same direction as their counterparts in EF3 and EF4 (Fig. 6E, inset).

In summary, the results from MD simulations suggest that the equilibrium between the open and the closed conformation of CaM variants is dependent on: i) the specific aminoacidic substitution, ii) the ion bound, and iii) the EF-hand motif(s) involved in the binding, either directly or via long-range allosteric effects, in line with the solvent exposure of basic residues observed in limited proteolysis experiments.

3.6. Effects of Pb^{2+} and arrhythmia-associated mutations on ion coordination assessed by MD simulations

Mutations in Ca^{2+}-sensor proteins may affect their ion-coordination capability, regardless of the direct involvement of the aminoacid in the ion-binding loop. We therefore monitored the solvent accessibility of the ions bound to CaM variants during the simulations, to evaluate potential effects of arrhythmia-associated variants on cation binding. The time-

evolution of the solvent accessible surface of the ions bound to WT CaM (Fig. 7 and Fig. S3) did not show any major variations over the 1 μs trajectories in all three conditions tested, with values never exceeding 20 Å^2, indicating that all ions remained bound to the respective EF-hand motif.

The same analysis performed on N53I CaM, on the other hand, highlighted an increase in solvent accessibility for the Ca^{2+}-ion bound to EF2 in the Ca^{2+}-loaded form (Fig. 7 and Fig. S4, left panel) to values reaching ~120 Å^2 after ~900 ns, which indicates that Ca^{2+}-coordination was completely lost. The dissociation of the Ca^{2+}-ion from EF2 was somehow surprising, since the N53I substitution was not directly involved in Ca^{2+}-coordination, but it affected one of the residues of the entering helix of EF2 (αE2, Fig. 1). This suggested that the alteration of the conformation of the EF2 motif would be ultimately responsible for the disruption of the bipyramidal pentagonal geometry necessary for retaining the Ca^{2+} ion in its position. No other variation in solvent accessibility for any ion bound could be noticed during the simulated timeframe for either the Pb^{2+}-loaded or the intermediate state (Fig. 7 and Fig. S4).

The Ca^{2+}-loaded N97S variant exhibited the same behavior as the N53I variant in the same state, with the Ca^{2+}-ion dissociating from EF2, although the loss of coordination of the ion occurred earlier, after ~575 ns (Fig. 7 and Fig. S5, left panel). At odds with the N53I variant, though, the disease-associated substitution affected residue N97, which directly participates to the Ca^{2+}-coordination in EF3 through its backbone carbonyl group, thus implying allostery as the mechanism underlying

the detachment of the Ca^{2+}-ion from EF2, which maps on the other protein domain. A similar mechanism could be invoked when analyzing the solvent accessibility of the Pb^{2+}-loaded form of N97S, where the dissociation of the Pb^{2+}-ion from EF1 occurred towards the end of the simulation (~990 ns, Fig. 7, and Fig. S5, middle panel), despite the mutation being in the C-terminal domain. Conversely, no ion dissociation from any EF-hand motifs could be detected for the intermediate form of the N97S mutation (Fig. 7 and Fig. S5, right panel), again with a solvent accessibility of the ions stably below ~30 Å^2.

The arrhythmia-associated variant exerting the most detrimental effect on ion coordination was found to be the E104A substitution, affecting the bidentate ion-coordinating residue of EF3. Indeed, ion dissociation from EF3 was detected in both the Ca^{2+}-loaded and the Pb^{2+}-loaded form (Fig. 7 and Fig. S6), although while the Ca^{2+}-coordination was lost after only ~345 ns (the lowest dissociation time among all tested variants), the solvent accessibility of the Pb^{2+}-ion reached ~120 Å^2 after ~655 ns. This finding was not surprising, as mutations affecting the bidentate Ca^{2+}-coordinating residues have been shown to be the most detrimental to Ca^{2+}-affinity in Ca^{2+}-sensor proteins [63–65].

Notably, in the Pb^{2+}-loaded form a second dissociation event occurred towards the end of the simulation (~925 ns), this time affecting the other EF-hand belonging to the C-terminal domain, namely EF4 (Fig. 7 and Fig. S6). Such dissociation events were surprisingly not detected for the intermediate state, which retained all ions bound to EF-hands like all other tested variants. However, it must be noticed that the
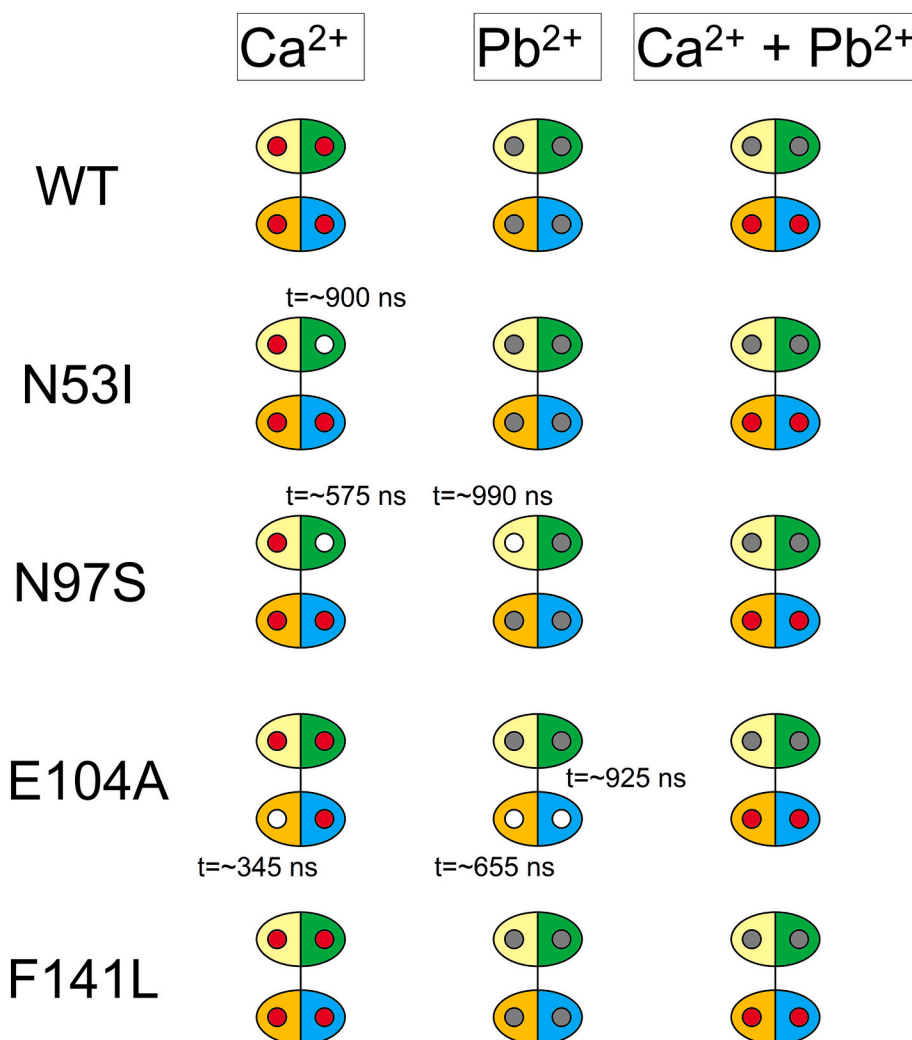
Fig. 7. Ion dissociation from CaM variants monitored by molecular dynamics simulations. CaM N- and C-lobes are represented as ellipses, EF-hand motifs are colored according to Fig. 1, namely EF1 in yellow, EF2 in green, EF3 in orange, EF4 in blue. Ca^{2+} and Pb^{2+} ions are represented as red and grey circles, respectively. White circles represent ion dissociation from the EF-hand motif, the simulation time at which the ion is released from the binding loop and thus completely solvent-exposed is reported.

intermediate state represents a transition phase, whose kinetics of association/dissociation events may not be properly sampled over the simulated timeframe. These results suggest that the E104A variant may alter the intradomain allosteric communication between EF3 and EF4, required for the physiological dynamics of Ca^{2+} binding [66] and recently found to be crucial for RyR1 and RyR2 target discrimination [51]. Finally, the F141L variant, affecting the first residue of helix αF4, did not affect ion coordination in any EF-hand of all three simulated conditions (Fig. 7 and Fig. S7).

Altogether, our findings indicate that the presence of arrhythmia-associated variants may exert allosteric effects on CaM flexibility, which reflects on the altered equilibrium between the open and the closed conformation. Ion binding was also found to be allosterically affected by CaM variants, although ion dissociation from the EF-hands in CaM variants N53I, N97S and E104A did not occur concomitantly with the conformational transitions between the open and closed conformation (Figs. 6 and 7), thus creating a conceptual distinction between ion binding (i.e. affinity) and conformational transition. A similar phenomenon was observed with recoverin, another EF-hand Ca^{2+} sensor [67–69].

3.7. Effects of Pb^{2+} on the affinity of CaM variants for RyR2 peptide monitored by intrinsic fluorescence spectroscopy

CaM is known to be able to interact with a plethora of targets, thus allowing the regulation of a variety of physiological processes [30], thanks to its high structural plasticity [57]. RyR2, responsible for

triggering the Ca^{2+}-induced Ca^{2+}-release during cardiomyocytes contraction [36], is one of such targets, and its regulation is known to be altered in the presence of a number of CaM missense mutations, among which those investigated in this study, ultimately resulting in sudden cardiac death [44–47]. In an attempt to assess potential synergistic effects, we probed whether Pb^{2+}-binding affected the molecular recognition of the WT CaM-RyR2 complex and whether the presence of variants N53I, N97S, E104A, and F141L exerted any synergistic effect on the affinity for the target.

To investigate the affinity of the CaM-RyR2 complex, we took advantage of the lack of Trp residues in CaM and of the presence of a unique Trp residue in RyR2 CaMBD2 peptide (residues R3581-L3611, RSKKAV**W**HKLLSKQRKRAVVACFRMAPLYNL) [48], and we monitored the variation in the wavelength of the maximal intrinsic fluorescence intensity upon titrating RyR2 peptide with CaM, in the presence of Ca^{2+} and upon addition of Pb^{2+}. The analysis of the titration curves highlighted that WT Ca^{2+}-loaded CaM bound RyR2 peptide with high affinity ($K_d = 331.0 \pm 8.8$ nM, Table 2), which was not affected by the presence of either N53I or N97S substitutions, as shown by their comparable K_d values (339.0 ± 47.3 and 333.5 ± 49.5 nM, respectively, Table 2), in line with previous results obtained at 25 °C by fluorescence titrations [70] and Isothermal Titration Calorimetry [71]. Interestingly, the K_d of WT CaM for RyR2 at 37 °C was almost 3-fold higher compared to previously published values obtained by performing the same experiment at 25 °C [51], highlighting the temperature-dependence of the CaM-RyR2 interaction.

E104A and F141L mutations, on the other hand, displayed
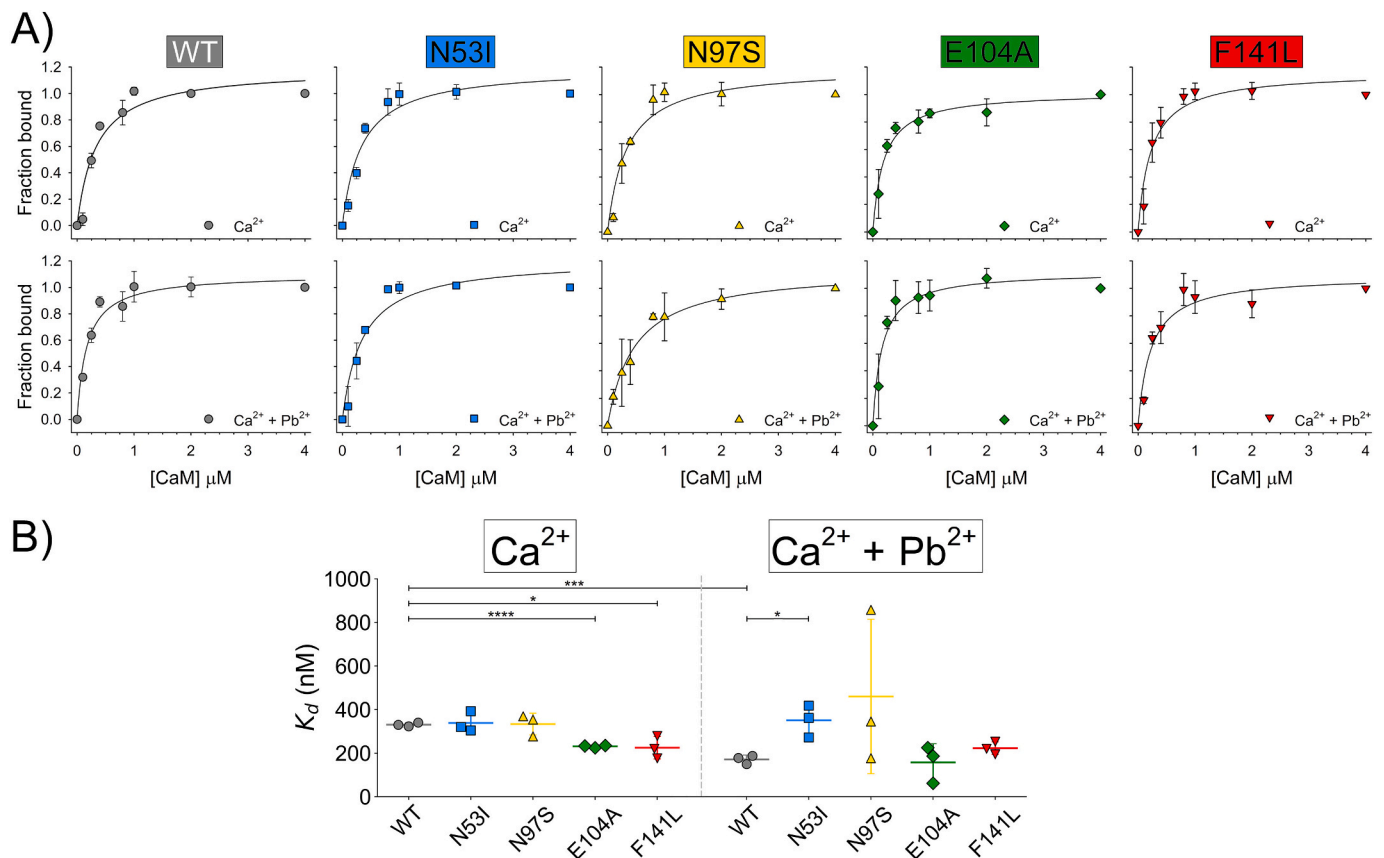
Fig. 8. Interaction between CaM and RyR2 assessed using fluorescence spectroscopy. A) Increasing concentrations of CaM (0–4 μM) were added in the presence of a fixed amount of RyR2 (1 μM) in the presence of 80 μM Ca^{2+} (A, upper panels) and after the addition of 80 μM Pb^{2+} (A, lower panels). Each titration was performed in triplicate at 37 °C, setting $\lambda^{ex} = 295$ nm and collecting emission spectra between 300 and 400 nm. Each spectrum represents the average of 3 accumulations, the results are showed as the fraction of the peptide bound as a function of CaM concentration and the obtained distribution fitted using a One-site Ligand Binding function. B) Scatter plot of the individual K_d calculated for each titration replica in the presence of sole Ca^{2+} (left) or in the co-presence of Ca^{2+} and Pb^{2+} (right). The statistical significance of the differences in K_d values was assessed by two-tailed t-tests, * p-value <0.05; ** p-value <0.01; *** p-value <0.001; **** p-value <0.0001.

significantly higher affinity compared to the WT (Fig. 8A, upper panels and Fig. 8B, left panel), with a K_d of 231.0 ± 5.5 and 225.1 ± 51.4 nM, respectively (Table 2), suggesting that the CaM-regulated Ca^{2+}-gating by RyR2 may be dysregulated due to the tighter interaction of the CaM-RyR2 complex in the presence of E104A and F141L variants. Surprisingly, N97I and Q135P variants, located in the same EF-hand as E104A (EF3) and F141L (EF4), respectively, were previously found to decrease CaM affinity for RyR2 compared to the WT, although in experiments performed at 25 °C [51], which on one hand suggests the altered target recognition as a potential pathological mechanism, on the other hand highlights that the affinity of CaM-RyR2 complex is strongly dependent on the specific mutation. On the same line, F141L was previously found not to significantly alter the affinity for RyR2 under Ca^{2+}-saturating conditions at 25 °C, pointing again towards temperature as an important factor to modulate CaM-RyR2 affinity [71,72].

In the presence of both Ca^{2+} and Pb^{2+}, WT CaM was found to interact more strongly with the RyR2 peptide (Fig. 8) with respect to the Ca^{2+}-loaded form, as its dissociation constant decreased to 171.7 ± 19.5 nM, the largest effect exerted by Pb^{2+} on CaM-RyR2 affinity among all tested variants. Surprisingly, addition of Pb^{2+} showed negligible effects on the affinity of N53I CaM for RyR2 ($K_d = 350.7 \pm 73.6$ vs 339.0 ± 47.3 nM, Table 2) compared to the Ca^{2+}-loaded state, although affinity was significantly lower compared to the WT under the same conditions ($K_d = 350.7 \pm 73.6$ vs 171.7 ± 19.5 nM, Fig. 8B, Table 2). The N97S mutation exhibited a WT-like affinity for RyR2 in the presence of only Ca^{2+}, with no statistically significant variations upon addition of Pb^{2+}, most probably due to the low reproducibility of the titration curves, which resulted in highly scattered K_d values (460.1 ± 354.5, Table 2). Finally, Pb^{2+} did not alter the affinity of either E104A or F141L substitutions compared to their Ca^{2+}-loaded counterparts in a statistically significant manner ($K_d = 157.9 \pm 85.3$ vs 231.0 ± 5.5 nM and 222.7 ± 28.9 vs 225.1 ± 51.4, respectively, Table 2); furthermore, the affinity for RyR2 exhibited by both variants was not significantly different from that of the WT in the same cation-loading state.

In summary, the alteration of CaM affinity for RyR2 due to arrhythmia-associated substitutions was found to depend on the specific variant, rather than on the structural location of the mutated residue. Indeed, in the presence of Ca^{2+}, although both N97S and E104A variants affect residues belonging to EF3, the former did not exhibit appreciable differences in affinity, whereas the latter displayed enhanced affinity for the target, as was the case for the F141L variant, localized in the adjacent EF4. Moreover, increased affinity for RyR2 exhibited by Ca^{2+}-saturated F141L and E104A variants was comparable to that measured for WT CaM in the presence of Pb^{2+}. We thus speculate that lead toxicity in otherwise healthy individuals may manifest in a perturbation of the CaM-RyR2 recognition similar to that found in patients with arrhythmia-associated variants, in the absence of Pb^{2+}.

CaM-RyR2 recognition is finely regulated by intra- and inter-domain interactions, which result in complex allosteric effects [50]. Future dedicated work is needed to clear up the emerged scenario.

4. Conclusions

In summary, our study demonstrated that Pb^{2+} can displace Ca^{2+} and alter WT CaM secondary structure, which acquires a coiled-coil super-secondary assembly. When bound to CaM, Pb^{2+} is hard to displace even in conditions of equimolar $[Ca^{2+}]$, thus locking CaM in a specific conformation. The presence of Ca^{2+} does not alter the dynamics of the secondary structure conformational rearrangement of CaM upon Pb^{2+} binding, although the secondary structure transition occurs at higher Pb^{2+} levels. In addition, the presence of arrhythmia-associated mutations shifts the conformational transition towards the coiled-coil conformation to lower Pb^{2+}, regardless of the presence of Ca^{2+}; MD simulations suggest that allosteric communication between the two domains may occur, even in the absence of a molecular target.

Finally, the significant increase in affinity of Pb^{2+}-bound WT CaM for RyR2, at least for the CaMBD2 region, suggests that both neuro- and cardio-toxic effects of Pb^{2+} mediated by CaM could perturb the molecular recognition process. However, when the analysis is extended to arrhythmia-associated variants, results clearly show that affinity, and thus equilibrium, is not sufficient to explain specific effects of pathogenetic variants, for which a synergistic effect with Pb^{2+} binding seems to be excluded for the interaction of this specific target.

Declaration of competing interest

The authors declare no conflict of interest. The funders had no role in the design of the study; in the collection, analyses, or interpretation of data; in the writing of the manuscript, or in the decision to publish the results.

Data availability

Data will be made available on request.

Appendix A. Supplementary information

Supplementary data to this article can be found online at https://doi.org/10.1016/j.bbamcr.2023.119490.

References

[1] P.B. Tchounwou, C.G. Yedjou, A.K. Patlolla, D.J. Sutton, Heavy metal toxicity and the environment, Exp Suppl 101 (2012) 133–164.

[2] P.K. Gautam, R.K. Gautam, S. Banerjee, M.C. Chattopadhyaya, J.D. Pandey, Heavy metals in the environment: fate, transport, toxicity and remediation technologies, in: D. Pathania (Ed.), Heavy Metals: Sources, Inc, Toxicity and Remediation Techniques, Nova Science Publishers, 2016, pp. 101–130.

[3] B. Wang, Y. Liu, H. Wang, L. Cui, Z. Zhang, J. Guo, S. Liu, W. Cui, Contamination and health risk assessment of lead, arsenic, cadmium, and aluminum from a total diet study of Jilin Province, China, Food Sci Nutr 8 (2020) 5631–5640.

[4] C.C. Bridges, R.K. Zalups, Molecular and ionic mimicry and the transport of toxic metals, Toxicol. Appl. Pharmacol. 204 (2005) 274–308.

[5] T.L. Dowd, J.F. Rosen, L. Mints, C.M. Gundberg, The effect of Pb(2+) on the structure and hydroxyapatite binding properties of osteocalcin, Biochim. Biophys. Acta 1535 (2001) 153–163.

[6] J. Bressler, K.A. Kim, T. Chakraborti, G. Goldstein, Molecular mechanisms of lead neurotoxicity, Neurochem. Res. 24 (1999) 595–600.

[7] C.M. Bouton, L.P. Frelin, C.E. Forde, H. Arnold Godwin, J. Pevsner, Synaptotagmin I is a molecular target for lead, J. Neurochem. 76 (2001) 1724–1735.

[8] C.S. Chetty, G.R. Reddy, K.S. Murthy, J. Johnson, K. Sajwan, D. Desaiah, Perinatal lead exposure alters the expression of neuronal nitric oxide synthase in rat brain, Int. J. Toxicol. 20 (2001) 113–120.

[9] M.J. Ronis, T.M. Badger, S.J. Shema, P.K. Roberson, F. Shaikh, Effects on pubertal growth and reproduction in rats exposed to lead perinatally or continuously throughout development, J Toxicol Environ Health A 53 (1998) 327–341.

[10] J.C. Aub, P. Reznikoff, Lead Studies, Iii., The effects of lead on red blood cells. Part 3. A chemical explanation of the reaction of lead with red blood cells, J. Exp. Med. 40 (1924) 189–208.

[11] F. Khalil-Manesh, H.C. Gonick, E.W. Weiler, B. Prins, M.A. Weber, R.E. Purdy, Lead-induced hypertension: possible role of endothelial factors, Am. J. Hypertens. 6 (1993) 723–729.

[12] C.V. Nolan, Z.A. Shaikh, Lead nephrotoxicity and associated disorders: biochemical mechanisms, Toxicology 73 (1992) 127–146.

[13] F.M. Johnson, The genetic effects of environmental lead, Mutat. Res. 410 (1998) 123–140.

[14] R. Gorkhali, K. Huang, M. Kirberger, J.J. Yang, Defining potential roles of Pb(2+) in neurotoxicity from a calciomics approach, Metallomics 8 (2016) 563–578.

[15] L. Shimoni-Livny, J.P. Glusker, C.W. Bock, Lone pair functionality in divalent Lead compounds, Inorg. Chem. 37 (1998) 1853–1867.

[16] C. Gourlaouen, O. Parisel, Is an electronic shield at the molecular origin of lead poisoning? A computational modeling experiment, Angew Chem Int Ed Engl 46 (2007) 553–556.

[17] T.J. Simons, G. Pocock, Lead enters bovine adrenal medullary cells through calcium channels, J. Neurochem. 48 (1987) 383–389.

[18] W.D. Atchison, Effects of toxic environmental contaminants on voltage-gated calcium channel function: from past to present, J. Bioenerg. Biomembr. 35 (2003) 507–532.

[19] C.S. Fullmer, S. Edelstein, R.H. Wasserman, Lead-binding properties of intestinal calcium-binding proteins, J. Biol. Chem. 260 (1985) 6816–6819.

[20] T.L. Dowd, J.F. Rosen, C.M. Gundberg, R.K. Gupta, The displacement of calcium from osteocalcin at submicromolar concentrations of free lead, Biochim. Biophys. Acta 1226 (1994) 131–137.

[21] H.A. Godwin, The biological chemistry of lead, Curr. Opin. Chem. Biol. 5 (2001) 223–227.

[22] P.L. Goering, Lead-protein interactions as a basis for lead toxicity, Neurotoxicology 14 (1993) 45–60.

[23] T.J. Simons, Lead-calcium interactions in cellular lead toxicity, Neurotoxicology 14 (1993) 77–85.

[24] G.W. Goldstein, Evidence that lead acts as a calcium substitute in second messenger metabolism, Neurotoxicology 14 (1993) 97–101.

[25] A. Persechini, N.D. Moncrief, R.H. Kretsinger, The EF-hand family of calcium-modulated proteins, Trends Neurosci. 12 (1989) 462–467.

[26] H. Ouyang, H.J. Vogel, Metal ion binding to calmodulin: NMR and fluorescence studies, Biometals 11 (1998) 213–222.

[27] M. Zhang, T. Tanaka, M. Ikura, Calcium-induced conformational transition revealed by the solution structure of apo calmodulin, Nat. Struct. Biol. 2 (1995) 758–767.

[28] R. Chattopadhyaya, W.E. Meador, A.R. Means, F.A. Quiocho, Calmodulin structure refined at 1.7 A resolution, J. Mol. Biol. 228 (1992) 1177–1192.

[29] J. Gsponer, J. Christodoulou, A. Cavalli, J.M. Bui, B. Richter, C.M. Dobson, M. Vendruscolo, A coupled equilibrium shift mechanism in calmodulin-mediated signal transduction, Structure 16 (2008) 736–746.

[30] F.C. Stevens, Calmodulin: an introduction, Can J Biochem Cell Biol 61 (1983) 906–910.

[31] J.L. Cox, S.D. Harrison Jr., Correlation of metal toxicity with in vitro calmodulin inhibition, Biochem. Biophys. Res. Commun. 115 (1983) 106–111.

[32] M. Kirberger, J.J. Yang, Structural differences between Pb2+− and Ca2+−binding sites in proteins: implications with respect to toxicity, J. Inorg. Biochem. 102 (2008) 1901–1909.

[33] M. Kirberger, H.C. Wong, J. Jiang, J.J. Yang, Metal toxicity and opportunistic binding of Pb(2+) in proteins, J. Inorg. Biochem. 125 (2013) 40–49.

[34] M.S. Alam, S. Azam, K. Pham, D. Leyva, K.J.D. Fouque, F. Fernandez-Lima, J. Miksovska, Nanomolar affinity of EF-hands in neuronal calcium sensor 1 for bivalent cations Pb2+, Mn2+, and Hg2, Metallomics 14 (2022).

[35] S. Azam, J. Miksovska, Pb(2+) binds to downstream regulatory element antagonist modulator (DREAM) and modulates its interactions with binding partners: A link between neuronal calcium sensors and Pb(2+) neurotoxicity, ACS Chem. Neurosci. 10 (2019) 1263–1272.

[36] J.T. Lanner, D.K. Georgiou, A.D. Joshi, S.L. Hamilton, Ryanodine receptors: structure, expression, molecular details, and function in calcium release, Cold Spring Harb. Perspect. Biol. 2 (2010), a003996.

[37] D.N. Hertle, M.F. Yeckel, Distribution of inositol-1,4,5-trisphosphate receptor isotypes and ryanodine receptor isotypes during maturation of the rat hippocampus, Neuroscience 150 (2007) 625–638.

[38] J. Nakai, T. Imagawa, Y. Hakamat, M. Shigekawa, H. Takeshima, S. Numa, Primary structure and functional expression from cDNA of the cardiac ryanodine receptor/calcium release channel, FEBS Lett. 271 (1990) 169–177.

[39] Y. Hakamata, J. Nakai, H. Takeshima, K. Imoto, Primary structure and distribution of a novel ryanodine receptor/calcium release channel from rabbit brain, FEBS Lett. 312 (1992) 229–235.

[40] Q. Jia, G. Du, Y. Li, Z. Wang, J. Xie, J. Gu, G. Yin, S. Zhang, Y. Gao, F. Zhou, C. Feng, G. Fan, Pb(2+) modulates ryanodine receptors from the endoplasmic reticulum in rat brain, Toxicol. Appl. Pharmacol. 338 (2018) 103–111.

[41] F. Zhou, G. Du, J. Xie, J. Gu, Q. Jia, Y. Fan, H. Yu, Z. Zha, K. Wang, L. Ouyang, L. Shao, C. Feng, G. Fan, RyRs mediate lead-induced neurodegenerative disorders through calcium signaling pathways, Sci. Total Environ. 701 (2020), 134901.

[42] G. Ferreira, A. Santander, L. Chavarria, R. Cardozo, F. Savio, L. Sobrevia, G. L. Nicolson, Functional consequences of lead and mercury exposomes in the heart, Mol. Asp. Med. 87 (2022), 101048.

[43] E.M. Capes, R. Loaiza, H.H. Valdivia, Ryanodine receptors, Skelet. Muscle 1 (2011) 18.

[44] H.H. Jensen, M. Brohus, M. Nyegaard, M.T. Overgaard, Human calmodulin mutations, Front. Mol. Neurosci. 11 (2018) 396.

[45] M. Nyegaard, M.T. Overgaard, M.T. Sondergaard, M. Vranas, E.R. Behr, L. L. Hildebrandt, J. Lund, P.L. Hedley, A.J. Camm, G. Wettrell, I. Fosdal, M. Christiansen, A.D. Borglum, Mutations in calmodulin cause ventricular tachycardia and sudden cardiac death, Am. J. Hum. Genet. 91 (2012) 703–712.

[46] K. Takahashi, T. Ishikawa, N. Makita, K. Takefuta, T. Nabeshima, M. Nakayashiro, A novel de novo calmodulin mutation in a 6-year-old boy who experienced an aborted cardiac arrest, HeartRhythm Case Rep 3 (2017) 69–72.

[47] L. Crotti, C.N. Johnson, E. Graf, G.M. De Ferrari, B.F. Cuneo, M. Ovadia, J. Papagiannis, M.D. Feldkamp, S.G. Rathi, J.D. Kunic, M. Pedrazzini, T. Wieland, P. Lichtner, B.M. Beckmann, T. Clark, C. Shaffer, D.W. Benson, S. Kaab, T. Meitinger, T.M. Strom, W.J. Chazin, P.J. Schwartz, A.L. George Jr., Calmodulin mutations associated with recurrent cardiac arrest in infants, Circulation 127 (2013) 1009–1017.

[48] K. Lau, M.M. Chan, F. Van Petegem, Lobe-specific calmodulin binding to different ryanodine receptor isoforms, Biochemistry 53 (2014) 932–946.

[49] P. Kursula, V. Majava, A structural insight into lead neurotoxicity and calmodulin activation by heavy metals, Acta Crystallogr Sect F Struct Biol Cryst Commun 63 (2007) 653–656.

[50] G. Dal Cortivo, C.G. Barracchia, V. Marino, M. D'Onofrio, D. Dell'Orco, Alterations in calmodulin-cardiac ryanodine receptor molecular recognition in congenital arrhythmias, Cell. Mol. Life Sci. 79 (2022) 127.

[51] G. Dal Cortivo, V. Marino, S. Bianconi, D. Dell'Orco, Calmodulin variants associated with congenital arrhythmia impair selectivity for ryanodine receptors, Front. Mol. Biosci. 9 (2023) 1100992.

[52] M.M. Bradford, A rapid and sensitive method for the quantitation of microgram quantities of protein utilizing the principle of protein-dye binding, Anal. Biochem. 72 (1976) 248–254.

[53] M.J. Abraham, T. Murtola, R. Schulz, S. Páll, J.C. Smith, B. Hess, E. Lindahl, GROMACS: high performance molecular simulations through multi-level parallelism from laptops to supercomputers, SoftwareX 1-2 (2015) 19–25.

[54] J. Huang, S. Rauscher, G. Nawrocki, T. Ran, M. Feig, B.L. de Groot, H. Grubmüller, A.D. MacKerell, CHARMM36m: an improved force field for folded and intrinsically disordered proteins, Nat. Methods 14 (2016) 71–73.

[55] V. Marino, S. Sulmann, K.W. Koch, D. Dell'Orco, Structural effects of Mg(2)(+) on the regulatory states of three neuronal calcium sensors operating in vertebrate phototransduction, Biochim. Biophys. Acta 2015 (1853) 2055–2065.

[56] R. Vallone, G. Dal Cortivo, M. D'Onofrio, D. Dell'Orco, Preferential binding of mg (2+) over ca(2+) to CIB2 triggers an allosteric switch impaired in usher syndrome type 1J, Front. Mol. Neurosci. 11 (2018) 274.

[57] A. Astegno, V. La Verde, V. Marino, D. Dell'Orco, P. Dominici, Biochemical and biophysical characterization of a plant calmodulin: role of the N- and C-lobes in calcium binding, conformational change, and target interaction, Biochim. Biophys. Acta 2016 (1864) 297–307.

[58] N.E. Zhou, C.M. Kay, R.S. Hodges, Synthetic model proteins: the relative contribution of leucine residues at the nonequivalent positions of the 3-4 hydrophobic repeat to the stability of the two-stranded alpha-helical coiled-coil, Biochemistry 31 (1992) 5739–5746.

[59] N. Choy, V. Raussens, V. Narayanaswami, Inter-molecular coiled-coil formation in human apolipoprotein E C-terminal domain, J. Mol. Biol. 334 (2003) 527–539.

[60] P. Zagel, D. Dell'Orco, K.W. Koch, The dimerization domain in outer segment guanylate cyclase is a ca(2)(+)-sensitive control switch module, Biochemistry 52 (2013) 5065–5074.

[61] S.R. Martin, P.M. Bayley, The effects of Ca2+ and Cd2+ on the secondary and tertiary structure of bovine testis calmodulin, A circular-dichroism study, Biochem J 238 (1986) 485–490.

[62] C. Holt, L. Hamborg, K. Lau, M. Brohus, A.B. Sorensen, K.T. Larsen, C. Sommer, F. Van Petegem, M.T. Overgaard, R. Wimmer, The arrhythmogenic N53I variant subtly changes the structure and dynamics in the calmodulin N-terminal domain, altering its interaction with the cardiac ryanodine receptor, J. Biol. Chem. 295 (2020) 7620–7634.

[63] V. Marino, G. Dal Cortivo, E. Oppici, P.E. Maltese, F. D'Esposito, E. Manara, L. Ziccardi, B. Falsini, A. Magli, M. Bertelli, D. Dell'Orco, A novel p., (Glu111Val) missense mutation in GUCA1A associated with cone-rod dystrophy leads to impaired calcium sensing and perturbed second messenger homeostasis in photoreceptors, Hum. Mol. Genet. 27 (2018) 4204–4217.

[64] G. Dal Cortivo, V. Marino, F. Boni, M. Milani, D. Dell'Orco, Missense mutations affecting Ca(2)-coordination in GCAP1 lead to cone-rod dystrophies by altering protein structural and functional properties, Biochim Biophys Acta Mol Cell Res 1867 (2020) 118794.

[65] J. Evenas, A. Malmendal, E. Thulin, G. Carlstrom, S. Forsen, Ca2+ binding and conformational changes in a calmodulin domain, Biochemistry 37 (1998) 13744–13754.

[66] S. Linse, A. Helmersson, S. Forsen, Calcium binding to calmodulin and its globular domains, J. Biol. Chem. 266 (1991) 8050–8054.

[67] V. Marino, M. Riva, D. Zamboni, K.W. Koch, D. Dell'Orco, Bringing the ca(2)(+) sensitivity of myristoylated recoverin into the physiological range, Open Biol. 11 (2021), 200346.

[68] D. Dell'Orco, S. Sulmann, S. Linse, K.W. Koch, Dynamics of conformational Ca2+− switches in signaling networks detected by a planar plasmonic device, Anal. Chem. 84 (2012) 2982–2989.

[69] D. Dell'Orco, M. Muller, K.W. Koch, Quantitative detection of conformational transitions in a calcium sensor protein by surface plasmon resonance, Chem Commun (Camb) 46 (2010) 7316–7318.

[70] M.T. Sondergaard, Y. Liu, W. Guo, J. Wei, R. Wang, M. Brohus, M.T. Overgaard, S. R.W. Chen, Role of cardiac ryanodine receptor calmodulin-binding domains in mediating the action of arrhythmogenic calmodulin N-domain mutation N54I, FEBS J. 287 (2020) 2256–2280.

[71] M.T. Sondergaard, Y. Liu, K.T. Larsen, A. Nani, X. Tian, C. Holt, R. Wang, R. Wimmer, F. Van Petegem, M. Fill, S.R. Chen, M.T. Overgaard, The arrhythmogenic calmodulin p.Phe142Leu mutation impairs C-domain Ca2+ binding but not calmodulin-dependent inhibition of the cardiac ryanodine receptor, J. Biol. Chem. 292 (2017) 1385–1395.

[72] M.T. Sondergaard, Y. Liu, M. Brohus, W. Guo, A. Nani, C. Carvajal, M. Fill, M. T. Overgaard, S.R.W. Chen, Diminished inhibition and facilitated activation of RyR2-mediated ca(2+) release is a common defect of arrhythmogenic calmodulin mutations, FEBS J. 286 (2019) 4554–4578.